Preparation of 2D Materials with Small Scale Multiphase Flows

by
Mohammad Jafarpour

Submitted to the Graduate School of Engineering and Natural Sciences
in partial fulfillment of the requirements for the degree of
Master of Science

Sabanci University
Spring 2021

Preparation of 2D Materials with Small Scale Multiphase Flows

APPROVED BY:

DATE OF APPROVAL: 05/07/2021

Preparation of 2D Materials with Small Scale Multiphase Flows

Mohammad Jafarpour

Mechatronics Engineering, MSc. Thesis, 2021

Thesis Supervisors: Prof. Dr. Ali Koşar and Dr. Morteza Ghorbani

ABSTRACT

Tremendous research efforts have recently focused on the synthesis of graphene from graphitic materials, while environmental issues, scalability, and cost are some of the major challenges to be surmounted. Liquid phase exfoliation (LPE) of graphene is one of the principal methods for this synthesis. Nevertheless, sufficient information about the mechanisms of exfoliation has yet to emerge. Here, a microreactor based on the hydrodynamic cavitation (HC) on a chip concept is introduced to exfoliate graphite in a totally green process which involves only natural graphite flakes and water. The present sustainable reactor system was found to exfoliate thick and large graphite particles to nano-sized sheets (~ 1.2 nm) with a lateral size of ~ 500 nm to 5 μm.

Besides the application of hydrodynamic cavitation for 2D material synthesis, in the second part of this thesis we tried to fabricate a filter/membrane for separating of gas or some component of liquid media with the use of electrospinning method. Electrospinning is an electrohydrodynamic process involving a polymeric droplet and slim charged liquid jet. The polymer solution is subjected to a high potential electric field. The high voltage enables the production of continuously long fibers on a collector surface. In this thesis, the effects of major parameters on the electrospun fibers were extensively investigated. Optimum conditions for electrospinning were obtained on the surface of a collector, and the diameter of resulting fibers, through SEM (Scanning Electron Microscopy) investigations, was determined. The optimum values for concentration, applied voltage, the distance between the tip of needle and collector, and flow rate determined to be 10 wt.%, 12 kV, 20 cm, and 0.6 $ml.h^{-1}$, respectively. Afterwards, the

hydrophilicity of fibers was modified by adding different poly (ethylene glycol) (PEG) concentrations (20, 30, and 40 wt.%) to the polymeric solution. The contact angle analysis revealed that the poly (methyl methacrylate) (PMMA) and 30 wt.% PEG fabricated fibrous mat exhibited a better wettability and lower hydrophobicity compared to pure PMMA electrospun mats. In the next step, silica NPs (nanoparticles) were introduced to the polymeric solution of electrospinning in the form of an IPA (isopropanol)-based collide solution. The dispersed solution-based addition of silica NPs prevented the aggregation state of NPs in the nanofibers. The addition of silica nanoparticles also changed the thermal and mechanical properties of the ternary composite, which were analyzed in TGA (thermogravimetric analysis) and tensile tests. These results highlight that the hybrid composite leads to a promising new electrospun mat for filtration and bioengineering applications.

Keywords: Graphene, Exfoliation, Hydrodynamic Cavitation, Electrospun Fibers; Membrane; Poly (methyl methacrylate**)**; Polyethylene glycol.

Küçük Ölçekli Çok Fazlı Akışlarla 2D Malzemelerin Hazırlanması

Mohammad Jafarpour
ME, M.Sc. Tezi, 2021
Tez danışmanı: Prof. Dr. Ali Koşar ve Dr. Morteza Ghorbani

ÖZET

Son zamanlarda yoğun araştırma çabaları, grafit malzemelerden grafen sentezine odaklanmıştır. Bu bağlamda çevresel sorunlar, ölçeklenebilirlik ve maliyet üstesinden gelinmesi gereken başlıca zorlukları teşkil etmektedir. Grafenin sıvı faz eksfoliyasyonu (LPE), bu sentez için temel yöntemlerden biridir. Bununla birlikte, pul pul dökülme mekanizmaları hakkında henüz yeterli bilgi ortaya konmamıştır. Bu tezde, yalnızca doğal grafit pulları ve su içeren tamamen yeşil bir işlemde grafiti pul pul dökmek için bir çip konsepti üzerinde hidrodinamik kavitasyona (HC) dayalı bir mikroreaktör geliştirilmiştir. Mevcut sürdürülebilir reaktör sisteminin, kalın ve büyük grafit parçacıklarını, yanal boyutu ~ 500 nm ila 5 um olan nano boyutlu levhalara (~ 1.2 nm) eksfoliye ettiği kanıtlanmıştır.

2D malzeme sentezi için hidrodinamik kavitasyon uygulamasının yanı sıra, bu çalışmanın ikinci bölümünde, elektroeğirme yöntemi kullanılarak gazın veya sıvı ortamın bazı bileşenlerinin ayrılması için bir filtre/membran geliştirilmiştir. Elektroeğirme, polimerik bir damlacık ve ince yüklü sıvı jeti içeren elektrohidrodinamik bir işlemdir. Polimer çözeltisi, yüksek potansiyelli bir elektrik alanına maruz bırakılır. Yüksek voltaj, bir kollektör yüzeyinde sürekli uzun liflerin üretilmesini sağlar. Bu tezde, ana parametrelerin elektrospun elyaflar üzerindeki etkileri kapsamlı bir şekilde araştırılmıştır. Elektroeğirme için optimum koşullar bir toplayıcı yüzeyinde elde edilmiş ve elde edilen liflerin çapı, SEM (Taramalı Elektron Mikroskobu) incelemeleri ile belirlenmiştir. Konsantrasyon, uygulanan voltaj, iğne ucu ile kollektör arasındaki mesafe ve akış hızı için optimum değerler sırasıyla ağırlıkça %10, 12 kV, 20 cm ve 0,6 ml.h-1 olarak belirlenmiştir. Daha sonra, polimerik çözeltiye farklı poli (etilen glikol) (PEG)

konsantrasyonları (ağırlıkça %20, 30 ve 40) eklenerek liflerin ıslanabilirliği modifiye edilmiştir. Temas açısı analizi, poli (metil metakrilat) (PMMA) ve ağırlıkça %30 PEG ile üretilmiş lifli matın, saf PMMA elektrospun matlarına kıyasla daha iyi bir ıslanabilirlik ve daha düşük hidrofobiklik sergilediğini ortaya koymuştur. Bir sonraki adımda, silika NP'ler (nanopartiküller), bir IPA (izopropanol) bazlı çarpışma çözeltisi formunda elektroeğirmenin polimerik çözeltisine dahil edilmiştir. Dağılmış çözelti bazlı silika NP'lerin eklenmesi, nanoliflerde NP'lerin topaklanma durumunu önlemiştir. Silika nanopartiküllerin eklenmesi, TGA (termogravimetrik analiz) ve çekme testlerinde analiz edilen üçlü kompozitin termal ve mekanik özelliklerini de değiştirmiştir. Bu sonuçlar, hibrit kompozitin filtrasyon ve biyomühendislik uygulamaları için umut verici yeni bir elektrospun mata yol açtığını vurgulamaktadır.

Anahtar Kelimeler: Grafen, Eksfoliasyon, Hidrodinamik Kavitasyon, Elektrospun Elyaflar; membran; Poli (metil metakrilat); Polietilen glikol.

Acknowledgments

First, I am really grateful to have chance to work under supervision of my thesis supervisors, Prof. Dr. Ali Koşar and Dr. Morteza Ghorbani and thankful for the continuous supports, guidance, encouragement, and immense knowledge.

I need to thank Prof. Dr. Fevzi Çakmak Cebeci and Dr. Mustafa Kamal Bayazit owning to transferring of his knowledge and deepening my eyesight in my thesis. Without their novel solutions and thorough knowledge, there was no way I can complete this projects. Also, my gratitude towards Prof. Dr. Yegan Erdem my thesis jury member, for her dedication and constructive comments for improving the technical context of the thesis.

This work was supported by TUBITAK (The Scientific and Technological Research Council of Turkey) Support Program for Scientific and Technological Research Project (Grant No. 119M495). Equipment utilization support from the Sabanci University Nanotechnology Research and Applications Center (SUNUM) is gratefully appreciated.

I would like to thank my fellow friends Dr. Araz Sheibani Aghdam, Moein Talebian Gevari, Farzad Rokhsar Talab Azar, Ali Ansari Hamadani, Taha Behroozi Kohlan, Milad Torabfam and all my colleagues in nanofluidic and microfluidic lab for their priceless help, whom I had the chance to know and collaborate with during the last two years of my academic life. They helped me to overcome all the difficulties and burdens on my way in completing this thesis.

Special thanks to my friends Vahid Charkhesht, Behnam Parizad Benam, Kamal Asadi Pakdel, Mirvahid Mohammadpour Chehreghani, Darya Farrokhnemoun, Taher Abbasiasl, Milad Shojaeaian, Kosar Hasannezhad, Sourush Niazi, Ali Hosseinpour Shafaghi, Nilufar Piruzfam, Amin Balazadeh, Shahrzad Sajjadivand, Peiman Khandar, and Nasser Pourmohammadi Vafa who have supported me along the way during my study at Sabanci University.

The last but not the least, I would like to express my everlasting grace to my family for supporting and encouraging me throughout my years of study and my life in general. This accomplishment would not have been possible without them.

Table of Contents

Table of Figures

Table of Tables

Chapter 1. Overview and Introduction

1.1 Introduction- Graphene Exfoliation Based on the "Hydrodynamic Cavitation on a Chip" Concept

2D nanomaterials have been extensively implemented for improvements in the quality of life since their discovery and exploitation. During the past decade, many research efforts have been focused on graphene due to its outstanding electrical, optical, chemical, and mechanical properties, as well as its unique 2D honeycomb lattice [1,2]. These unique characteristics have attracted the attention of many researchers so that the scope of the research on graphene has been broadened beyond materials engineering and physics [3]. In this regard, a substantial number of studies on drug delivery [4,5], nanoelectronics [6,7], batteries and fuel cells [8,9], sensors [10,11], and supercapacitors [12] were recently published.

Production of graphene and related materials at a reasonable cost from graphite is a long-lasting scientific challenge and puts an obstacle against graphene-based emerging applications. The properties of graphene and related materials are closely related to their synthesis method, which could enable the precise control of their shape, size, and surface properties, thereby leading to versatile physical, chemical, and biomedical characteristics [13]. Over the years, various methods have been proposed to produce graphene, which can be categorized into two major approaches: top-down and bottom-up [14]. Top-down approaches involve the separation of the stacked layers of graphite into graphene sheets. Mechanical exfoliation [15,16], liquid-phase exfoliation (LPE) [17,18], unzipping of multi-wall carbon nanotubes (MWCNTs) [19,20], and arc discharge [21,22] are some examples of this approach. In contrast to top-down methods, bottom-up methods involve synthesizing graphene from carbon-containing sources such as chemical vapor deposition [23,24], epitaxial growth [25], and pyrolysis [26].

In general, in top-down methods, the process involves mechanical and chemical energies to break down weak Van der Waal forces in high-purity graphite sheets [27,28]. Typically, the mechanical routes for exfoliation of flakes apply in the form of two forces. The vertical impacts act on the flakes, which causes to overcome energy between layers to peel them apart (normal force), and the sliding relative movements between layers occur due to the exerted lateral force (shear force).

LPE, one of the most widely used top-down methods for graphene production, was first introduced in 2008. In this method high energy sonication or mixing are conducted to exfoliate graphite to graphene sheets in a solvent with addition of surfactants to avoid oxidation or reduction. On the other hand, spontaneously exfoliation of graphene sheets under the effect of high energy liquid-liquid interface is another approach, where graphite particles act as a surfactant in chemical-free medium [29,30]. Generally, there are three main steps in LPE synthesis: (i) dispersion of graphite in a suitable solvent, (ii) exfoliation, and (iii) purification of the final products [31]. In the second step, the formation and collapse of bubbles on the flake surfaces instantly result in a compressive stress wave propagation throughout the particle. Based on the theory of stress waves, the particle is also exposed to a reflected tensile stress wave. The cycle of creation and collisions of bubbles leads to intensive tensile stress in the flakes. Additionally, the other potential scenario is the exertion of unbalanced lateral compressive stress. This kind of stress can also break down adjacent layers by the shear effect [32]. As a result, it is an efficient and fast approach to develop nano-sized particles, where the prominent role belongs to cavitation bubbles [33].

Cavitation is a phase change phenomenon involving the nucleation, growth, and collapse of gas or vapor-filled bubbles in liquids [34,35]. The collapsing bubbles (cavities) in the liquid provide the energy source to initiate and enhance a wide range of chemical processes and introduce physical effects to break down graphite layers into graphene [36]. The resulting bubble collapse could generate very high energy densities (energy per unit volume), which causes a rise in the local temperature and pressure as large as 5000 K and 500 atm, respectively, over an extremely short period of time [37]. In general, acoustic-based exfoliation is carried out with an ultrasonic water bath or probe-tip sonicator, which can be scaled up to no more than a few hundred milliliters [38]. Indeed, because of the inefficient energy transfer from the source to the liquid medium, the increase in the volume will exacerbate the production rate. Thus, exfoliation of graphite to graphene by ultrasonication is not a suitable way for large scale graphene production [39].

Due to the significance of hydrodynamic cavitation in fluidic systems, many studies have been dedicated to provide an understanding about the effects of major parameters such as thermophysical properties of the working fluid, geometry of the reactor, and surface roughness elements [40,41]. Recently, the generation of

hydrodynamic cavitating flows in microfluidic devices has gained much attention because of the scalability, cost-effectiveness, and energy-efficiency. Furthermore, facile flow generation processes besides the stationary section of hydrodynamic reactors make them even more popular and effective [42,43].

Some studies on liquid exfoliation inside a microreactor are capable of generating hydrodynamic cavitation. For example, Liu et al. [44] attempted to prepare single and few-layered graphene flakes in a cavitation reactor by employing a water-acetone mixture. Their process yield was 4%, and they introduced this method as a promising mass production tool with advantages of low cost and green process. In one of the recent studies conducted by Qiu et al. [45], a 50 gL-1 graphite suspension with a sufficient amount of surfactant (Sodium Cholate) was processed by passing around 2000 times through a microreactor (~ 3 hours). The hydraulic power and relative energy consumption of their system were about 5W and 2 MJL-1, respectively. They reported that the surfactant might undergo destruction under intense cavitation, which can prevent the increase in the yield of process. In another study, graphene and its analogues materials were produced by the use of liquid phase exfoliation and microreactor, where Yi et al. [46] introduced the fluid dynamics method for scalable and efficient production. They performed the experiments with the help of a high-pressure plunger pump, and the suspensions were under the effect of *N, N*-Dimethylformamide (DMF) as a dispersion medium. They treated the working fluid in 5-cycles.

Motivated by the emerging studies on LPE in microfluidic devices, herein, a sustainable hydrodynamic cavitation reactor system with a nozzle, which lead to a sudden decrease in the cross-sectional area of the fluid path and an increase in the velocity of the working fluid, was designed. This system was shown to be highly efficient in the large-scale preparation of stable graphene solutions from natural graphite powder in water. Accordingly, we developed an eco-friendly hydrodynamic cavitation induced microreactor, which could exfoliate graphene with the use of just pure water instead of harmful and expensive solvents and chemicals.

1.2 Introduction- Electrospinning of Ternary Composite of PMMA-PEG-SiO_2 Nanoparticles

The development of nano-scale and advanced multifunctional composite materials has been a growing subject of interest in materials science and nanotechnology [47]. Among the fabrication techniques, electrospinning has been rapidly emerging as a viable technique due to its simplicity, efficiency, low cost, and consistency in fabricating fibers, whose diameter could be reduced to tens of nanometers [48,49]. Electrospinning is an electrohydrodynamic process, where a high voltage is applied to generate a slim charged liquid jet followed by stretching the jet and solidifying continuously long fibers on a collector [50–52]. In general, the fabrication of electrospun fibers and control of their properties depend on several parameters, which can be divided into three main groups: electrospinning parameters, solution properties, and ambient conditions [53,54].

Electrospinning process parameters include the applied potential, flow rate of the solution, needle tip to collector distance, and needle diameter [55,56]. Solution properties are related to solvent volatility, concentration, polymer molecular weight, surface tension, dielectric constant, and conductivity [57,58]. The ambient conditions of the chamber, including humidity and temperature as well as other parameters, affect the morphology of final fibers [59]. Generally, the electrospinning process is a flexible process, where many different types of polymers such as water-soluble, water-insoluble, and composite materials could be prepared in the form of nanofibers mats [60,61]. These nonwoven structures have attracted great interest in various fields and applications, including filtration and wastewater treatment [62,63], biomedical and tissue engineering [64,65], sensors and catalysts [66,67], and energy storage [68,69] due to their high surface area to volume ratio, biocompatibility, porous networks, high permeability, and different types of surface morphology and modifications.

Among the polymers, poly(methyl methacrylate) (PMMA) has been widely used in many fields, as mentioned earlier. It is a glassy and non-water-soluble polymer, which possesses decent processing, biocompatibility, and inherent hydrophobicity [70,71]. However, the application of this material is constrained by its brittleness and low mechanical properties. Research efforts have been made to modify the fiber's surface morphology and the influence of electrospinning parameters on the fiber properties [72]. For instance, Liu et al. [70] reported the solvent's effect on fabricated fiber morphology for water treatment application. Their study showed that the surface wettability of the

PMMA fibers could be controlled by just adjusting the ratio of *N*,*N*-dimethylacetamide, and acetone in a binary solvent system. Ni et al. [73] attempted to fabricate the reinforced composite nanofibers of PMMA using cellulose nanocrystals (CNC). They reported that morphology, surface roughness, and tensile strength of PMMA composite nanofibers improved by adding CNC, and the further addition of CNC caused a decrease in the diameter of the fibers. In one of the recent studies conducted by Li et al. [74], the experimental results exhibited an enhancement in the composite membranes' maximum adsorption capacity and mechanical strength with chitosan addition to PMMA. The hydrogen bond formation between chitosan and PMMA was reported as the reason for the enhancement. In another study on the field of energy, Fu et al. [75] fabricated electrospun poly(vinylidene fluoride) (PVDF) membranes, where PMMA and SiO_2 nanoparticles (NPs) were introduced into the system to generate a PVdF/PMMA/SiO_2 composite membrane. The homogenous distribution of SiO_2 NPs on the electrospun fibers, along with a hot-pressing process, resulted in a high value of tensile strength (32.69 MPa) and high elongation at the fracture point.

To meet some application requirements, such as filtration and biomedical membranes, the mechanical properties and wettability of the electrospun mats should be adjusted [76,77]. The hydrophobic membranes usually cause clogging and flux-decline due to trapped air pockets within the mats. Thus, filters with a high-water contact angle are undesirable for filtration purposes [77,78]. The performance of the nanofibrous membranes could be improved by increasing the hydrophilicity of the fibers. Several methods have been reported to modify the surface hydrophobicity, such as applying a suitable hydrophilic material as a coating, grafting monomers to the surface of fibers, and blending hydrophilic additives to the system [79–81].

Blending a second component (polymer) is one of the most efficient and straightforward approaches for modulating the hydrophobicity of the fabricated membrane [82]. Poly(ethylene glycol) (PEG) is an ideal polymer to improve the wetting properties of nanofibers due to its hydrophilicity, solubility in water and organic solvents, and biocompatibility [50,82,83]. Tan et al. [84] studied the electrospun composite nanofibers of cellulose acetate butyrate (CAB) and PEG. Their study revealed that 10 to 20% of PEG in a 30% (w/v) of CAB and PEG concentration played an essential role in wettability and mechanical stiffness improvements. In another study, Kiani et al. [85] explained the effect of different PEG concentrations on the fabricated mat, whose

characteristics such as water contact angle and tensile strength had great importance in the filtration applications. According to their results, incorporating 10 wt.% of PEG in polyphenylsulfone enhanced the mechanical strength, decreased the water contact angle to 8.9°, and accordingly increased the water flux up to 7920 L/m^2h.

Besides the wettability enhancements by mixing the PMMA with a second polymer, several studies were conducted to reveal the effects of adding nanoparticles such as TiO_2 [86], SiO_2 [87], Al_2O_3 [88], ZrO_2 [89], SiC [90], CNTs [91], and graphene [92] into the polymeric electrospun fibers. These nanoparticles were used to control the fibers' surface roughness and mechanical properties and improve their chemical properties by functionalizing the nanoparticles. An essential point to note is the nanoparticle dispersion uniformity in the polymeric electrospinning solution and fabricated composite mat [76].

SiO_2 nanoparticles (NPs) as an inorganic material exhibit promising properties such as high mechanical strength, heat stability, chemical durability, and functionalizibility due to the presence of silanol groups in their structure [76,93,94]. Moreover, the addition of mesopores and macropores silica NPs increases the surface roughness of fibers [95]. Although the addition of NPs could improve the tensile strength of the composite, the added amount should be optimized to prevent the decrease in the toughness and elongation of the mat at fracture strain [50]. Qing et al. [96] reported the development of Silica/PVA nanofibrous membranes for oil/water separation. They reported that silica NPs generated a multi-scale roughness on the PVA membrane and improved its wettability. The fabricated filters showed high wettability in the air and underwater superoleophobicity properties based on the successful strategy for surface modification. Chen et al. [97] studied solutions of 20 wt.% of colloidal silica in methyl ethyl ketone (MEK), which was mixed with the electrospinning dimethylformamide (DMF) base solution to form uniformly distributed SiO_2 NPs in electrospun fibers. The fabricated fiber average diameter decreased to 350 nm by introducing SiO_2 NPs, adjusting the DMF/MEK ratio, and adding an ammonium salt. Furthermore, the thermal properties and surface hydrophilicity of composite nanofibers were improved and compared to the PMMA fibers.

Multi-component materials based on the electrospinning process have been developed because of their enhanced properties which could be promising to implement in a vast variety of fields such as bioengineering [98], filtration [99], and sensors [100],

where different nanoparticles were added to produce fibrous mat with improved performance which by one component electrospun nanofibers it is not achievable.

The emerging studies on fabrications of a nanocomposite fibrous mat based on PMMA in DMF-based solutions suggest that blending the PMMA with PEG and adding colloid silica NPs in isopropyl alcohol (IPA) assist in modifying the surface of fibers as well as mechanical property improvements. These combinations of different characteristics of mentioned materials offer superior properties such as hydrophilicity, water insolubility, and higher mechanical strength to PMMA. In this thesis, the effects of electrospinning parameters and concentration of PMMA on the formation of electrospun fibers were systematically investigated. Also, surface wettability transition due to the addition of PEG besides the effect of silica NPs on the mechanical strength of the fibers was studied for potential applications such as gas filtration membranes. The gas filtration is mainly related to the existence of ether groups in the PEG chemical structure, which will be our future study on the performance of fabricated electrospun mats.

Chapter 2. A Chemical-Free Process for Graphene Exfoliation Based on the "Hydrodynamic Cavitation on a Chip" Concept

2.1 Materials and Methods

2.1.1 Chemicals and Materials

Natural graphite powder was purchased from Alfa Aesar (Graphite flake, natural, -10 mesh, LOT: U24E068). The graphite solution with 25 mg L^{-1} solid concentration was prepared using de-ionized water without the use of any surfactant or dispersant agent. In a typical experiment, graphite flakes in water were sonicated using an ultrasonic bath sonicator (Bandelin Sonorex, Rangendingen, Germany) for 30 min. The resulting graphite solution was kept on a side for 15 min to precipitate out the unstable large graphite flakes, and the supernatant (*so-called as 'the starting graphite dispersion'*) was separated to be used in the hydrodynamic cavitation reactor, where it was passed through the reactor.

2.1.2 Microfluidic Device Geometry and Fabrication

The microfluidic device (hydrodynamic cavitation reactor) used in this thesis was fabricated using the semiconductor microfabrication techniques on silicon and was bonded to a glass cover to make sure that the reactors are leakproof. Thus, a fixed upstream pressure can lead to a stable flowrate in the reactors. The fabricated reactor consists of three main regions, namely inlet, nozzle, and extension zone. The widths of the inlet and extension are identical, while the width of the nozzle is smaller so that a sudden decrease in the flow cross-sectional area can be achieved.

According to the Bernoulli's principle, velocity and static pressure are inversely related. Hence, the increase in the fluid velocity as a result of the change in geometry of the flow restrictive element in the reactor leads to a decrease in the static pressure, which triggers the formation of cavitating flows.

Since the energy released from the collapsing bubbles provides the input of our system, it is vital to make sure that the majority of the bubble collapse occurs inside our reactor. For this purpose, the nozzle length in our reactor is significantly longer than the available studies in the literature, which facilitates the pressure recovery within the

system. Hence, the bubbles face a relatively high-pressure region in the extension area of the reactor, which results in the collapse within the reactor. The second feature of the fabricated reactor lies on the engineered wall of the nozzle area, where roughness elements were formed. Our previous studies reported that the presence of roughness elements on the walls facilitated the formation of cavitating flows [101]. The microfluidic device in this thesis is also equipped with wall roughness elements so that hydrodynamic cavitation can incept at lower upstream pressures. The reactor is resistant to high pressures and can withstand very high upstream pressures up to 1200 psi.

As mentioned before, the microfluidic device in this thesis consists of three regions with the same length of 2000 μm. The widths of inlet and extension zones are 900 μm, while this value for the nozzle is 400 μm. $2/3L_n$ of the nozzle length is equipped with triangular roughness elements with a height of 4 μm. One inlet and two outlets are formed on the reactor to realize the flow path. The detailed geometrical parameters of the microfluidic device are listed in Table 1.

Table 1. The geometrical characteristics of the reactor

Physical Configuration	**Range**
Nozzle length (L_n)	2000 μm
Nozzle width (W_n)	400 μm
Hydraulic diameter (D_h)	233 μm
Extension region length	2000 μm
Extension region width	900 μm
Length of the roughness elements (L_R)	$2/3\ L_n$
Height of the roughness elements (H_R)	$0.01\ W_n$

The process flow of the fabrication of the reactor in this thesis is the repetition of material deposition, patterning, and material removal using the standard microfabrication techniques. Accordingly, a layer of silicon dioxide was deposited on a double-side-polished silicon wafer. The inlet and outlet ports were patterned on the surface by the photolithography and dry etching processes. Then, second photolithography and deep reactive ion etching (DRIE) were performed on the wafer to obtain the final design. The

silicon wafer was then bonded anodically to a glass cap to finalize the nozzle configurations. Three pressure ports were patterned on the surface along with the inlet and outlet ports to assist in the measurements of the static pressure at the inlet, nozzles, and extension zones. More detailed information about the fabrication process flow can be found in our previous studies [102].

2.1.3 Preparation of Graphene Nanosheets

Graphene nanosheets were prepared using a hydrodynamic cavitation reactor system (shown in Figure 1a), which was constructed in similar lines with our previous studies [101]. The working fluid (the starting graphite dispersion) was kept in a stainless-steel container (1 gallon), which was connected to a high-pressure pure nitrogen tank, was introduced to the system via proper fittings and stainless-steel tubing. The microfluidic device was installed and sandwiched into a homemade aluminum package, which facilitated flow visualization and prevented any leakage. The sandwich holder consists of one inlet connected to the fluid container and one outlet, where the fluid leaves the reactor. The pressure sensors (Omega, Manchester, UK) were also installed on the package to measure the static pressures at three different locations of the reactor. A double-shutter CMOS high-speed camera (Phantom v310) along with a macro camera lens with a focal length of 50 mm was used to record the flow patterns during the experiments, while the volumetric flowrate of the system was measured at different upstream pressures.

The prepared solution was introduced to the tubing system by applying the upstream pressure supplied by the nitrogen tank. The solution was propelled to the hydrodynamic cavitation reactor, where the exfoliation process happened in the nozzle and extension regions. The increase in the upstream pressure leads to a faster fluid flow in the system. One of the major parameters, Reynolds number, is expressed as:

$$\mathrm{Re} = \frac{\rho V D_h}{\mu} \tag{1}$$

where ρ and μ are the fluid density and dynamic viscosity, respectively. The density of water at 20 °C is 998.2 kg/m^3, and the dynamic viscosity is 1cP in this thesis. Since the concentration of the graphite suspension is low, its effect on the density and viscosity of this working fluid is neglected. The velocity of the system, on the other hand, is calculated from the measured volumetric flow rate and cross-sectional area. D_h is the

hydraulic diameter of the nozzle. Cavitating flow characterization is of great importance to assess the intensity and flow pattern formation. For this purpose, the cavitation number is used and defined as:

$$\sigma = \frac{(P_i - P_{vap})}{0.5\rho V^2} \quad (2)$$

where P_i is the upstream pressure, P_{vap} is the saturation vapor pressure of the working fluid, V is the characteristic velocity of the fluid in the reactor, which is calculated at the beginning of the nozzle based on the volumetric flow rate of the system (flow rate/cross-sectional area).

2.1.4 Characterization methods

After different cycles of hydrodynamic cavitation, the collected samples were subjected to sequential centrifugations (Allegra X-15R, Beckman Coulter, Fullerton, CA, USA) to remove any unexfoliated material. The procedure for the sequential centrifugations is given in the Discussion section. The optical microscopy, Raman spectroscopy, scanning electron microscopy (SEM), and atomic force microscopy (AFM) for the samples were performed by transferring several drops of the supernatant (the top two-thirds of the dispersion from S3U samples) of second centrifuged suspension on silicon wafer substrates. The microscopic size and morphology of graphite/graphene were characterized by optical microscopy (Leica DM2700 M, Germany) and SEM (FE-SEM, LEO Supra VP-55, Germany). SEM images were taken after coating a very thin layer of gold-palladium alloy to observe the physical morphology and thickness of existing layers of the graphene. AFM measurements of graphene were made under ambient conditions at 60% relative humidity and 22 °C with a Digital Instruments Bruker multimode 8 in tapping mode. The characterization was obtained using a NanoAndMore tip with a bending spring constant of 40 Nm^{-1}, resonance frequency of 50‑200 kHz, and tip radius of 10‑20 nm. UV-Visible measurements were conducted on the samples in disposable cuvettes using a double-beam device (Varian Cary 5000 UV/Vis-NIR spectrometer) in the range of 200−800 nm. Raman spectroscopy was performed on a Renishaw inVia Reflex with the laser frequency of 532 nm as an excitation source. Raman spectra were obtained and normalized from at least 15 different spots on each sample. The size distribution of flakes after the specific cycles was determined using the dynamic light scattering (DLS) method. In this method, 1 ml of each sample was characterized in

disposal cuvettes. The experiment was carried out with a Zetasizer Nano ZS (Malvern Instruments) device equipped with a He/Ne laser operating at 633 nm as a light source.

2.2 Results and discussion

Graphene nanosheets were produced in the hydrodynamic cavitation reactor system (Figure 1a), where a top-down approach was adapted, and natural graphite flakes were exfoliated by energy released from the collapse of the cavitation bubbles. It is worth noting that the hydrodynamic cavitation-assisted production of graphene nanosheets in water is a green and sustainable process since it does not use any kind of chemicals such as surfactants and/or stabilizers.

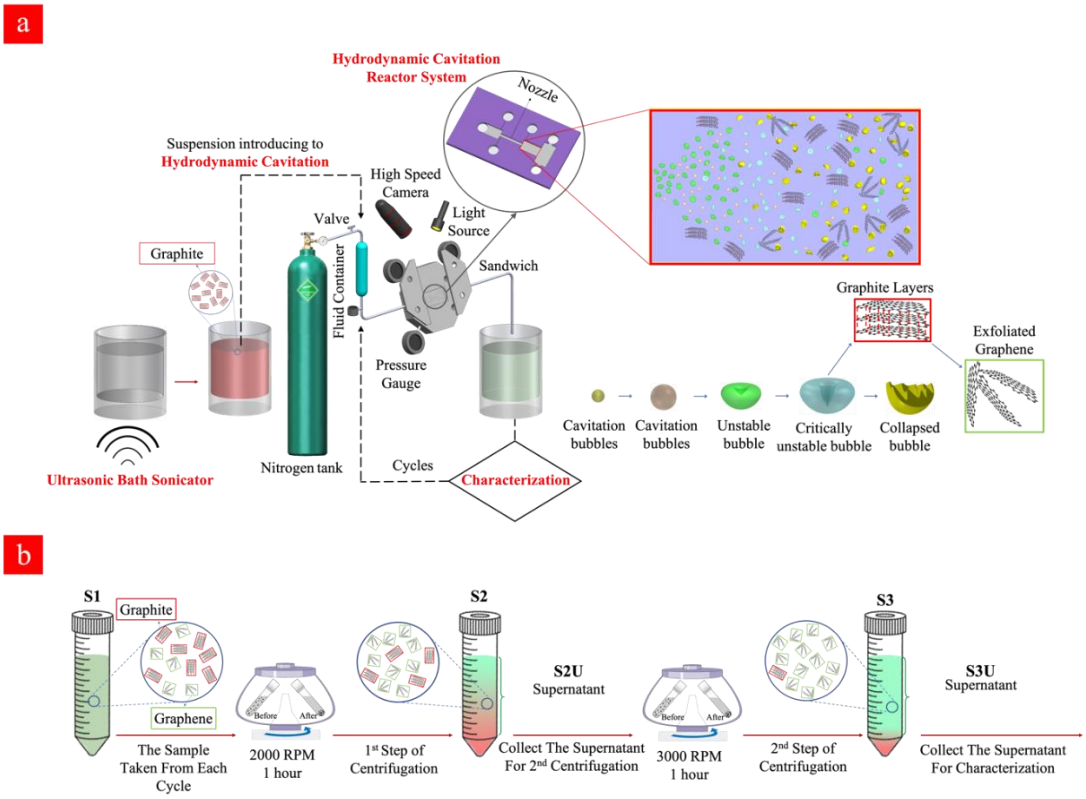

Figure 1. a) The schematic of the hydrodynamic cavitation reactor system for the production of graphene nanosheets, and b) The sequential centrifugation method for the isolation of the stable graphene nanosheets produced in the hydrodynamic cavitation reactor system.

In this process, graphite particles act as a solid interface in the working fluid and facilitate the heterogeneous bubble nucleation so that the process had low input energy for cavitation generation. The method is a fast and energy-efficient production method,

where the aqueous dispersions of graphite are treated through the cavitation setup, and the process lasts just a few seconds. The current hydrodynamic cavitation reactor system relying on a single nozzle microreactor is able to produce ~3.125 mg of graphene in a day, however, the production may be scaled up from milligrams to kilograms by engineering parallel multichannel chips with multi-nozzle microreactors.

2.2.1 Hydrodynamic cavitation and flow patterns

Under cavitating flow conditions, the static pressure at the nozzle area drops to a critical value due to a sudden change in the flow geometry. The high-speed camera system captures cavitating flows at the beginning of the nozzle area. The upstream pressure (P_i) corresponding to cavitation inception is 350 psi. The corresponding flow velocity is 68.2 m/s, while the corresponding Reynolds number can be found as 15861. Thus, it is evident that the flow is turbulent even at cavitation inception.

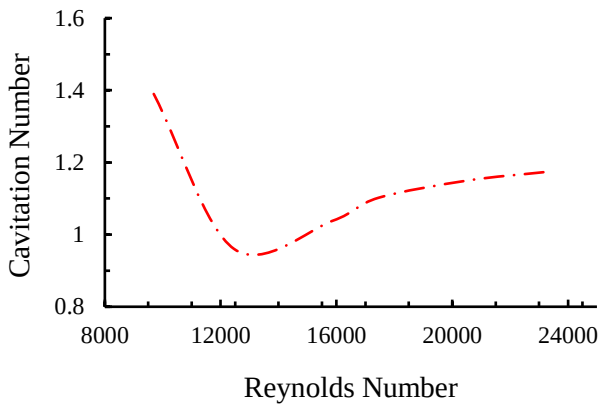

Figure 2. Cavitation number as a function of Reynolds number at different applied pressures.

Four main cavitating flow regimes could be observed under different conditions, namely, inception, developed flow, supercavitation, and choked flow. The inception of the cavitating flow appears when the gas phase is generated and corresponds to the weakest cavitating flow and largest cavitation number. With a gradual increase in the upstream pressure, the velocity increases so that the cavitation number follows a decreasing trend. At some points, when the reactor is saturated with the fluid flow, the velocity does not increase any more with the upstream pressure. Beyond this point, the cavitation number has an increasing trend, which corresponds to the choked flow regime. A moderate cavitation number (between inception and supercavitation flow regimes),

where the gas phase is elongated along the nozzle are, leads to the developed flow regime (Figure 2).

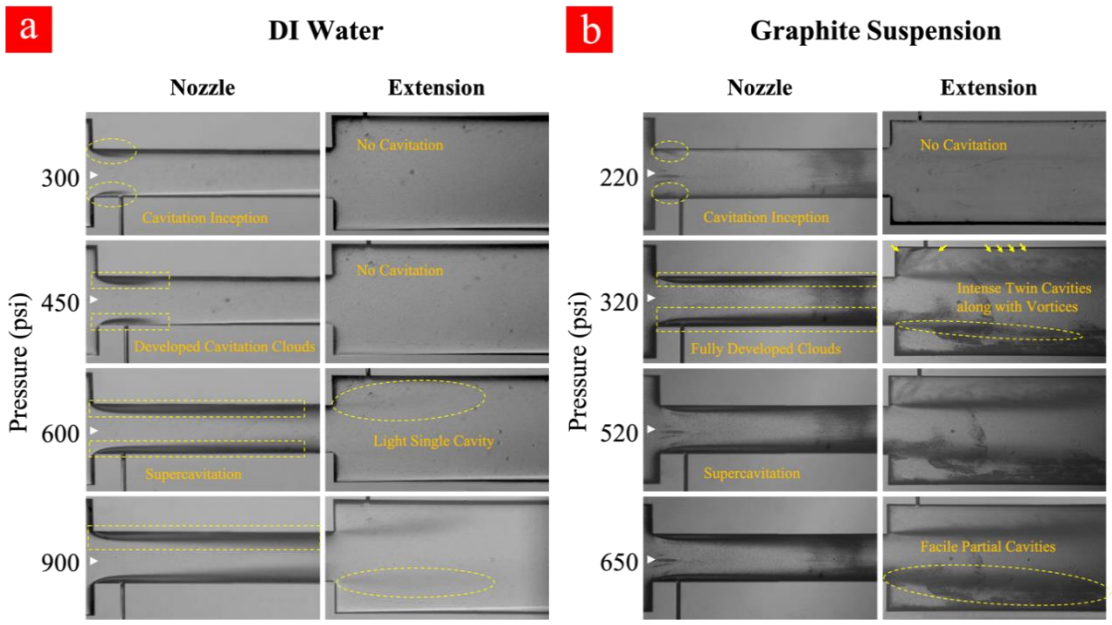

Figure 3. Different cavitation flow patterns at various upstream pressures for a) water and b) graphite suspension.

As can be seen in Figure 3, the upstream pressure for the case of graphite suspension is lower for the identical cavitating flow patterns. This observation can be explained by the increased number of heterogeneous nucleation sites in this case of suspensions. The presence of graphite particles in the working fluid acts as a solid/liquid interface. The micro-scale roughness elements on the surface of the graphite particles act as further heterogeneous nucleation sites, which can facilitate the inception and development of the cavitating flows.

Regarding the application of the fabricated microfluidic device in this thesis, developed flow regime corresponding to the upstream pressure of 650 psi is suitable for cyclic treatment of the graphite suspension and subsequent exfoliation due to the optimum conditions regarding the input power and output of the process. The experiments include 0-80 cycles so that the graphite suspension is thus treated with cavitating flows. Cavitating flows corresponding to inception and developed flow after the 80th cycle are shown in Figure 4. As shown in this figure, the cavitation inception decreases from 220 psi (first cycle) to 140 psi at the 80th cycle, while fully developed cavitating flow is seen at the upstream pressure of 300 psi. This indicates that more heterogeneous sites as a

result of the fine exfoliation are formed inside the introduced suspension, and the nucleation is triggered more vigorously after the 80th cycle.

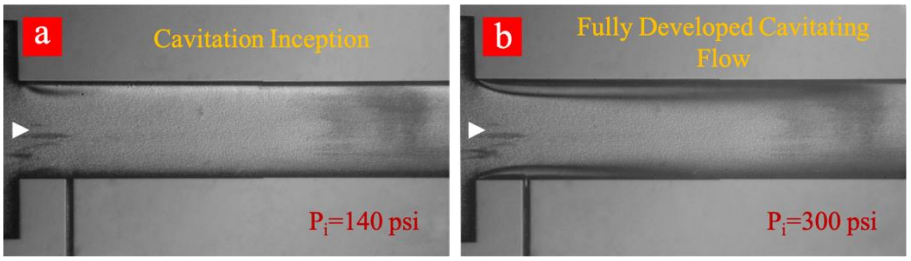

Figure 4. Inception and developed cavitating flow pattern for the graphene suspension after 80-cycles of hydrodynamic cavitation. a) the inception begins at 140 psi, and b) the fully developed cavitation flow pattern at 300 psi.

2.2.2 Characterization of Graphene Nanosheets

In the hydrodynamic cavitation-assisted graphene production process, the starting graphite dispersion was circulated through the system to evaluate the effect of the number of cycles on graphene production. The pre-defined cycles of 20, 40, 60, and 80 were used to study this effect. For example, to prepare a graphene-containing solution via 20-cycles, the starting graphite dispersion was circulated 20 times through the hydrodynamic cavitation system, and the obtained solution of the graphene nanosheets was analyzed using spectroscopic and microscopic techniques. To maintain the homogeneity in the produced graphene nanosheets, a sequential centrifugation method was developed and applied for all samples. In this method, the graphene dispersions after the hydrodynamic cavitation treatment were first centrifuged at 2000 rpm for 1 hour; thus, the exfoliated graphene nanosheets and small fragments of graphite were obtained in the supernatant solution (S2U). This supernatant was subjected to a second centrifugation process at 3000 rpm for 1 hour to remove large particles and to isolate the highly exfoliated stable graphene nanosheets (S3U). Figure 1b depicts a schematic for the isolation of the stable graphene nanosheets.

The isolated graphitic materials and the starting graphite dispersion were first characterized by Raman spectroscopy to evaluate the effect of the hydrodynamic cavitation on the exfoliation of graphite flakes. Raman spectroscopy is a versatile tool to analyze the structure of carbon nanomaterials, including carbon nanotubes [103,104] and graphene [105,106]. In a typical Raman spectrum of graphene, there are three commonly

reported peaks as D, G, and 2D bands at around 1350, 1580, and 2700 cm^{-1}, respectively [107]. The D band in the spectrum is related to the structural disorders, edges, and topological defects in the flakes. The area ratio of D-band to G-band (A_D/A_G) is often used to define the relative amount of surface defects on the graphene [108,109]. Besides, the 2D-band for graphene is attributed to two-phonon double resonance and can be used as a measure to evaluate the number of layers in the graphene nanosheets. More specifically, the intensity ratio of 2D-band to G-band band (I_{2D}/I_G) is an indication for the number of layers of graphene.

Figure 5 displays the Raman spectra of S3U-20, S3U-40, S3U-60, S3U-80, and the starting graphite dispersion. It is known that the position and shape of the 2D-band are highly sensitive to the number of graphene layers (less than 10 layers) because of the relations of peak activation parameters of Raman mode and band structure [110]. No significant change is observed in the maxima of the 2D-band of the S3U-20, S3U-40, and S3U-60 compared to the starting graphite dispersion (2D-band ~2716 cm^{-1}). However, there is a significant downshift (~25 cm^{-1}) in the maximum of the 2D-band for the S3U-80 and, the band appeared at 2692 cm^{-1}. In agreement with the literature [106], the observed shift can be attributed to the formation of bilayer graphene nanosheets after 80-cycles of hydrodynamic cavitation. Furthermore, the enhanced I_{2D}/I_G ratio after 80 -cycles further supports the formation of a few layer graphene nanosheets [111].

When the defect density was analyzed, almost no defect was observed for the starting graphite dispersion. In contrast, the isolated graphene nanosheets have I_D/I_G ratios of 0.10, 0.48, 0.32, and 0.87 for the S3U-20, S3U-40, S3U-60, and S3U-80, respectively, suggesting a gradual defect formation [112].

The nature of defects in graphene was previously studied [113], and it was shown that the intensity ratio between the D-band and D'-peak (at ca. 1620 cm^{-1}) could be used as a measure to probe the nature of the defects. In general, this ratio ($I_D/I_{D'}$) was found to be ~13 for sp^3-defects, while it was ~7 and ~3.5 for vacancy-like defects and boundaries in graphite, respectively. After the application of hydrodynamic cavitation, the intensity of D'-peak gradually increases with an increase in the number of cycles. In parallel, as above-mentioned, the intensity of D-band~ 1620 cm^{-1} also gradually increases. The isolated graphene nanosheets have $I_D/I_{D'}$ of 1.93, 2.31, 1.91, and 3.63 for the S3U-20, S3U-40, S3U-60, and S3U-80, respectively. From the observed ratios, it can be concluded

that the hydrodynamic cavitation creates surface defects on the exfoliated graphene nanosheets, and the defect density becomes more pronounced after 80-cycles of cavitation. However, it is worth pointing out that the calculated $I_D/I_{D'}$ ratios are lower than the ratios reported for the graphene nanosheets with sp^3 and vacancy-like defects.

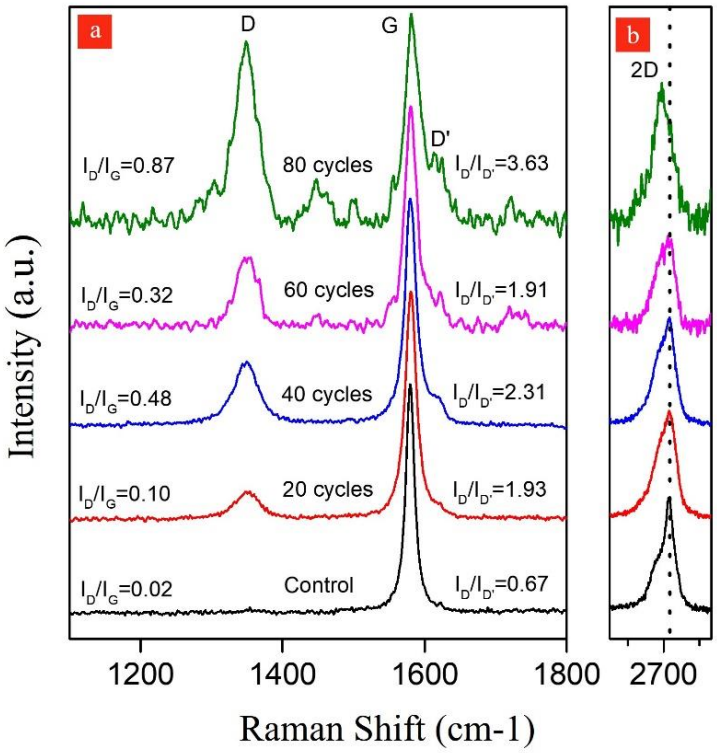

Figure 5. The normalized and offset Raman spectra (at G-band) of the produced graphene nanosheets after different cavitation cycles within the reactor. a) D-, G- and D'-band region of the Raman spectra b) 2D-band region. The dotted line in part b shows the shift in the position of the 2D-band after 80-cycles of cavitation.

The atomic force microscopy (AFM) characterization was used to determine the size and thickness of produced graphene nanosheets. The results complement the Raman spectroscopy data. AFM image and height profile of the produced graphene nanosheets after 80-cycles of hydrodynamic cavitation further confirm the exfoliation of graphite flakes into bi-layer graphene nanosheets having a thickness value of ~1 nm (Figure 6a). The thickness range of the produced graphene nanosheets after 60-cycles is approximately between 1.2 and 2.5 nm, which is considered as ≤3 layer graphene (Figure 6b) [114]. The lateral size of the analyzed nanosheets is in the range of 1-5 µm. Furthermore, close inspections on the AFM image of the few-layer graphene nanosheets produced after 60-cycles display large holes, which vary in sizes between 100 to 600 nm

(Figure 6c). The presence of these holes correlates well with the I_D/I_G ratios obtained by Raman spectroscopy, suggesting the formation of defects at the edges. These defects are not surprising since the exfoliated graphene nanosheets were subjected to intense cavitation energy. As in the LPE process, the formation of defects in the forms of edges and topological defects is unavoidable because these types of defects need lower formation energy. Furthermore, the size of the defects is believed to be related to the size of bubbles, which varies from hundreds of nanometers to micrometers.

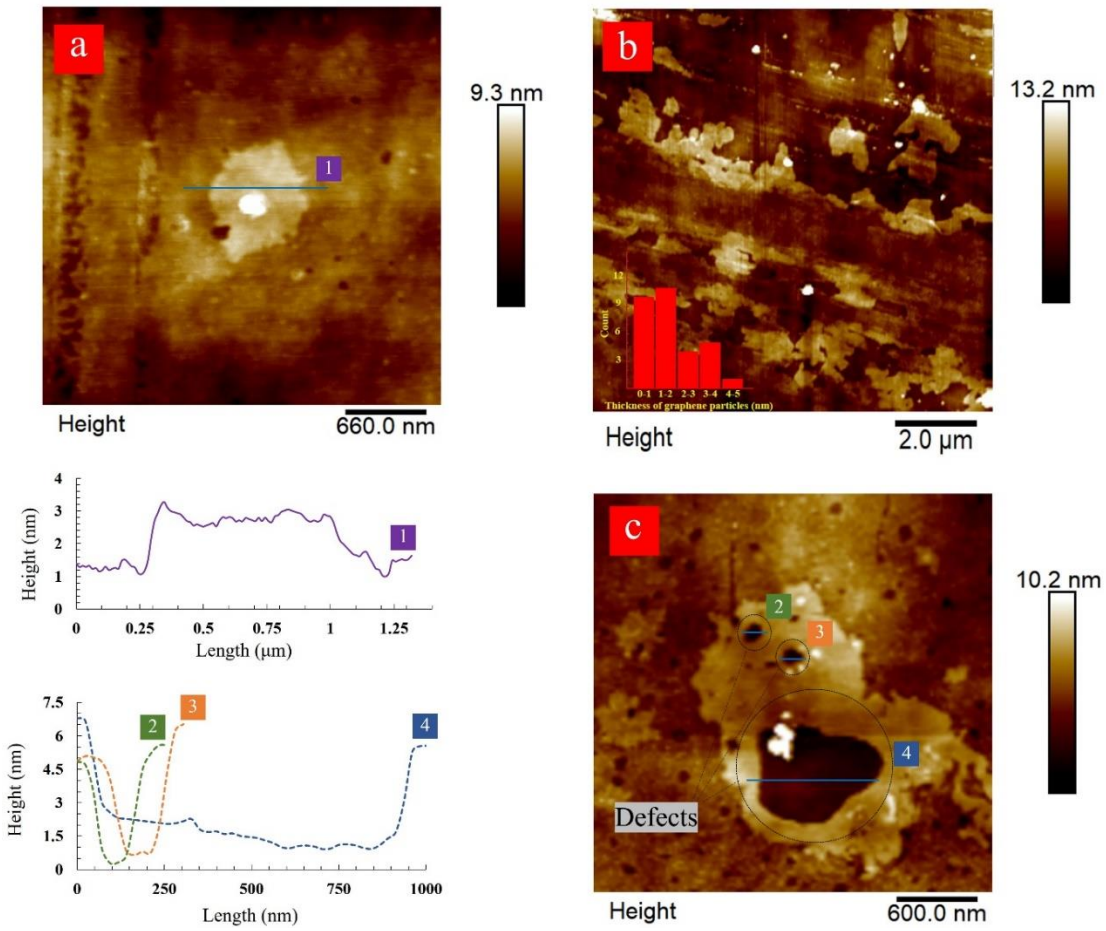

Figure 6. AFM images of monolayer and few layers of graphene sheets. a) a graphene sheet with a thickness about ~1 nm after 80-cycles, b) the exfoliated graphene nanosheets large in lateral size after 60-cycles of treatment, and c) a graphene sheet with defects, which were formed by exposure to excessive bubble collapse after 60-cycles.

UV-Vis spectroscopy was performed to assess the concentration of the isolated graphene nanosheets and the starting graphite dispersion. In agreement with the literature, the absorption spectra of the isolated graphene nanosheets (S3U-20 to 80) are featureless in the measurement range. Compared to the concentration of the starting graphite dispersion (25 µg mL^{-1}), the concentrations of the obtained graphene nanosheets are

calculated as ~2.1 (S3U-20), 1.1 (S3U-40), 1.0 (S3U-60), and 1.1 (S3U-80) μg mL^{-1} using the molar absorption coefficient of 3620 mL mg^{-1} m^{-1} at the wavelength of 660 nm for the graphene in water [115]. Using the concentrations of the isolated graphene nanosheets, the process efficiencies after 20-, 40-, 60-, and 80-cycles are calculated as 8.4%, 4.8%, 4%, and 4.4%, respectively. It is worth noting that the efficiency of the hydrodynamic cavitation-assisted graphene production process after 40-cycles is higher than the previously reported study [112]. However, the yield of exfoliated graphene showed a fast decrease after 20-cycles. The observed concentration loss may be related to the trapping of exfoliated graphene in the cavities and the porosities of the system. The efficiency of the system can be improved by reducing the length of the pipes, porosities of the exposed surfaces, and using a closed-loop system. Moreover, the UV-Vis analysis of a control sample prepared by centrifuging the starting graphite dispersion exhibits almost no absorbance at 660 nm (1.4 μg mL^{-1}). This result indicates that the stability of the isolated graphene nanosheets is higher than that of the starting graphite dispersion, probably due to the size shortening of graphite flakes.

The size distribution of the isolated graphene nanosheets was studied using the dynamic light scattering (DLS) technique. The DLS results of the centrifuged samples of carbon-based (graphite/graphene) colloids at the end of different hydrodynamic cavitation cycles are demonstrated in Figure 7. From the DLS data, it can be deduced that the mean diameter size of the particles gradually decreases with the increase in the number of hydrodynamic cavitation cycles. The mean particle size of the flakes in the starting graphite dispersion after two sets of centrifugation steps is measured as 3150 (±335) nm. Nevertheless, the measured particle sizes of S3U-20, S3U-40, S3U-60, and S3U-80 are 2744, 2242, 1664, and 1353 nm, respectively. The differences between the mean particle sizes are well-correlated with the number of hydrodynamic cavitation cycles. Complementary optical microscopy images are illustrated this fragmentation and size differences.

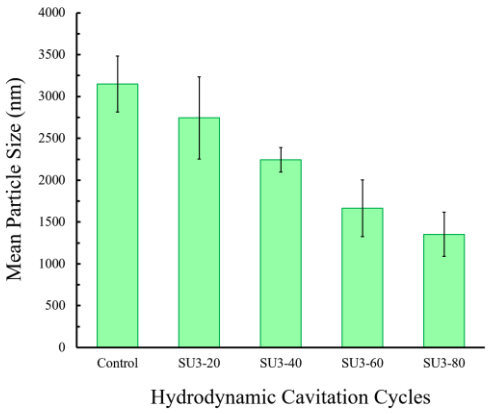

Figure 7. The measured average particle size of the hydrodynamic cavitation (20, 40, 60, and 80-cycles) treated and non-treated graphene nanosheets after two centrifugation steps.

The scanning electron microscopy (SEM) image of the starting graphite dispersion displays large flakes having a lateral dimension of over ~5 µm (Figure 8a). The lateral flake sizes of the isolated graphene sheets after 60 and 80-cycles decrease to ~4 and ~3 µm, respectively. The treatment by the reactor under the developed cavitating flow pattern causes changes in the graphite lateral size, and the SEM results are in good agreement with the DLS size distribution as well as the AFM data.

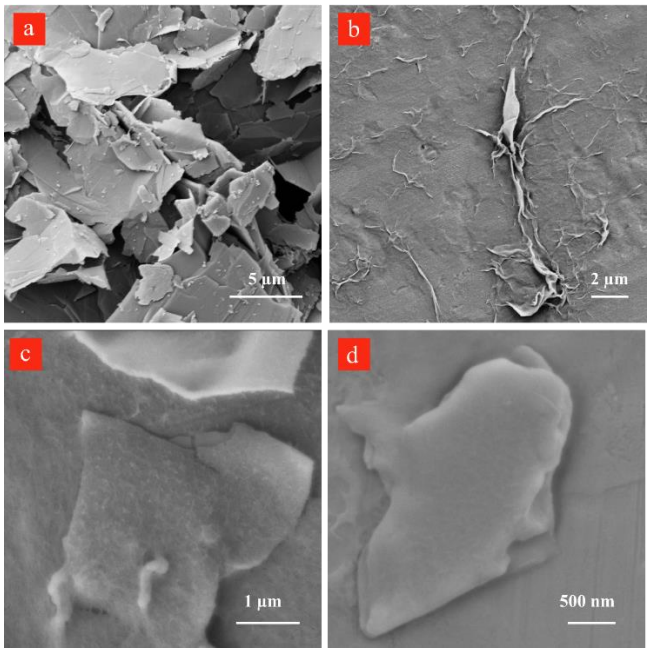

Figure 8. SEM images of a) the starting graphite dispersion, the graphene nanosheets obtained after sequential centrifugation of b) 60-cycles in low magnification, c) 60-cycles in higher magnification, and d) 80-cycles cavitation-treated graphite dispersion.

The residence time of the fluid in the hydrodynamic cavitation device is rather short (2.9×10^{-6} s). Therefore, the energy density ($E=J/m^3$) can be calculated using the pressure differential along the channel [116]. All of the cycles were performed at 650 psi (4.48×10^{6} J/m^3) for having consistent results. However, the pressure sufficient to have graphene exfoliation decreases to 300 psi (2.06×10^{6} J/m^3) with the number of cycles due to exfoliation and fragmentation of graphite powder in lower cycles, which provides active sites for nucleation of the cavitating bubbles. Figure 9 shows the graphene exfoliation yield as a function of energy density and compares hydrodynamic cavitation with the sonication and shear methods reported in the literature [117,118]. The results on hydrodynamic cavitation show a higher yield by consuming a lower energy density for graphene exfoliation. As a well-known technique for graphene exfoliation, sonication consumes 25-540 Watts of power (5 times more than hydrodynamic cavitation) for an extensive amount of time (3000 times more than hydrodynamic cavitation) to exfoliate a fraction of 1 liter of graphite solution [115,119–122]. Although the size of used graphite powders limits the hydrodynamic cavitation method, 300 times more energy is required to achieve the same yield for the sonication method.

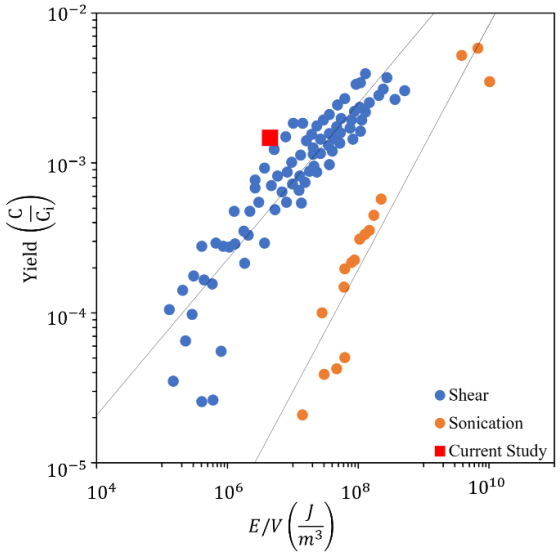

Figure 9. Graphene exfoliation yield as a function of energy density with the use of shear, sonication, and hydrodynamic cavitation exfoliation

Chapter 3. Electrospinning of Ternary Composite of PMMA-PEG-SiO_2 Nanoparticles: Comprehensive Process Optimization and Electrospun Properties

3.1 Materials and method

3.1.1 Chemicals and Materials

Polymethyl methacrylate (PMMA, M_w=350,000 g/mol), Poly(ethylene glycol) (average M_n~400), N,N-Dimethylformamide (≥99%), Tetraethyl Orthosilicate (TEOS), Ammonia hydroxide solution 25%, and 2-Propanol (IPA, 99.5%) were purchased from Sigma Aldrich (technical grade) and were used without any purification.

3.1.2 Silica nanoparticles synthesis

Mesoporous silica nanoparticles were synthesized by the simple one-step synthesis modified Stöber method [123]. In this method, tetraethyl orthosilicate (TEOS) as the precursor was introduced to an alcoholic solution to be hydrolyzed with the water in the ammonia solution. The hydrolyzed precursors, which lost the EtOH groups on their structure, link together to create larger molecules and finally build up silica nanoparticles. In this thesis, five batches of synthesizing baths with [TEOS]/[NH3]aq ratios of 4, 4.8, 6, 8, and 12 were prepared to control the particle size of silica NPs.

3.1.3 Solution preparation and electrospinning

Solutions of PMMA in DMF with a polymer/solvent ratio of 10 and 12.5 w/w% were prepared and electrospun to investigate the effects of electrospinning parameters and polymer concentration on the surface coverage and fibers diameter. Electrospinning was conducted using a plastic syringe fitted with a metallic needle (inner diameter of the needle was 1 mm) at the accelerating voltages of 12 to 20 kV. The distance between the needle tip and fixed stainless-steel collector (11×11 cm^2) varied from 5 to 20 cm, and the flow rates were set in a range of 0.3 to 0.9 $ml.h^{-1}$. After obtaining the optimum conditions for PMMA electrospinning and the best polymer/solvent ratio (10 wt.%), three different polymer blends of PMMA- 20 wt.%, 30 wt.%, and 40 wt.% PEG with the fixed polymer/solvent ratio of 10 wt.% were electrospun and characterized.

In the final step, silica NPs solutions (the synthesized method is explained in the next section) were added to electrospinning solution (with respect to fixed solid and powder: polymer ratios as 7.5 wt.% and 10:90, respectively). All the electrospinning experiments were conducted at 22.7 °C and relative humidity of 48%. The prepared solutions were stirred overnight at 55 °C before the electrospinning process to obtain homogeneous solutions.

3.1.4 Characterization

A double-shutter CMOS high-speed camera (Phantom v310, at 125 μs intervals (8,000 fps)) along with a macro camera lens was employed to take images of the bending instability of the electrospun jets. The Field Emission Scanning Electron Microscopy (FE-SEM, LEO Supra VP-55) was used to evaluate the electrospun fibers and silica NPs morphology and size. The samples were sputter-coated with Au/Pd before imaging. Quantitative nanoscale mechanical (QNM) characterizations were performed using the Bruker MultiMode VIII Scanning Probe Microscope under ambient conditions at scan rates of 0.5-1 Hz. The spring constant of cantilever was measured as 25 N/m using the thermal tuning method [124] and the tip radius was measured as 17 nm. The Derjaguin–Muller–Toporov (DMT) modulus [125] was analyzed using the Nanoscope Analysis software. The surface coverage, fiber diameter, and size distribution of fibrous mats were determined using the ImageJ software (National Institutes of Health, MD, USA). The silica NPs size distribution was assessed by the Dynamic Light Scattering technique (DLS) using the Malvern Zetasizer Nano ZS device equipped with a He/Ne 633 nm laser light source. Thermal Gravimetric Analysis (TGA) was carried out by heating the samples with a rate of 10 °C/min from room temperature to 800 °C by the NETZSCH STA 449 C instrument.

The chemical characterization of the fabricated composite fibers was performed using the Fourier transform infrared spectroscopy Nicolet iS10 spectrometer (Thermo Fisher Scientific Inc.) equipped with a universal attenuated total reflection (ATR) accessory. The samples were scanned from 500 to 4000 cm−1. Dynamic contact angle measurements of deionized distilled water were conducted using the Attension Theta Lite. Samples were placed on the instrument's specimen holder, and a 5 μL droplet of water hanging from the tip of the needle was placed gently on the surface of the sample. The droplet's contact angle was observed using a video camera. The mechanical tests were

performed using a Mark-10 ESM 303 motorized tension/compression test stand and M7-025 digital force gauge based on ASTM D882 - 10 standard test method for tensile properties of thin plastic sheeting with a thickness of less than 1 mm. The samples were cut in 40 x 10 mm dimensions and sandwiched in a 40 × 40 mm paper frame, as shown in Figure 10. The paper frame was cut after fixing the sample in the grips, and then the test was performed at a strain rate of 5 mm/min.

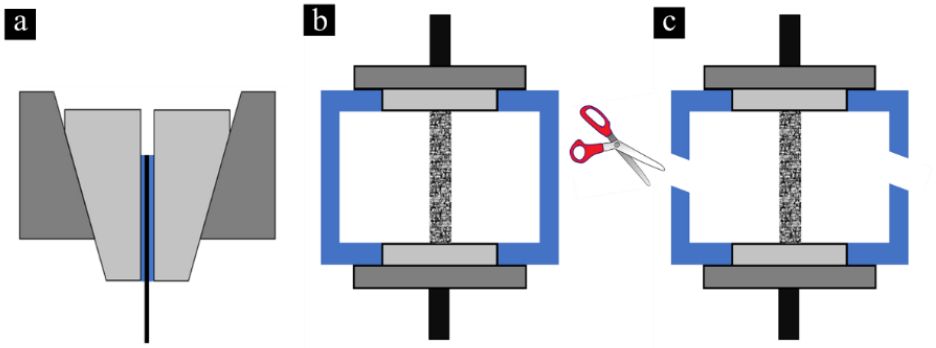

Figure 10. Preparation of a frame before the tensile test. The samples were cut in 40 x 10 mm dimensions and sandwiched in a 40 × 40 mm paper frame a) The fibrous mat between a frame was held within grip, b) the system was stretched until the frame became ready to do the analysis, and c) the frame was cut to start the test.

3.2 Results and discussion

3.2.1 Fiber diameter and morphology

The effect of the parameters, namely solution concentration, accelerating voltage, flow rate, and the needle tip to collector distance, on the fibrous mat surface coverage and mean diameter of fibers are investigated by considering 72 different combinations of the parameters. Figure 11 shows the surface coverage percentage of the electrospun fibers analyzed by the ImageJ software. In these diagrams, the optimum conditions for better coverage of the surface of the collector with nanofibers are shown with red color. Accordingly, the fiber mats cover less than 60% of the collector surface for the 12.5 wt.% polymer/solvent solution. The polymeric solution viscosity increases with an increase in the concentration to 12.5 wt.% polymer/solvent, which leads to a lower surface coverage. The low coverage could be explained by the higher viscoelastic force of the formed liquid jet, which resists the tension force during the electrospinning process [126]. The lower concentration (10 wt.%) gives rise to the generation of a stable jet, and bead-free mats can be obtained besides other optimized parameters such as applied potential, distance, and flow rate. The electrospun fibers using this solution at the flow rates of 0.6 and 0.9

ml.h^{-1} exhibit a sizeable red region (80-100 % coverage) on their profiles. However, the flow rate of 0.3 ml.h^{-1} was insufficient to provide enough material to cover the surface of the collector.

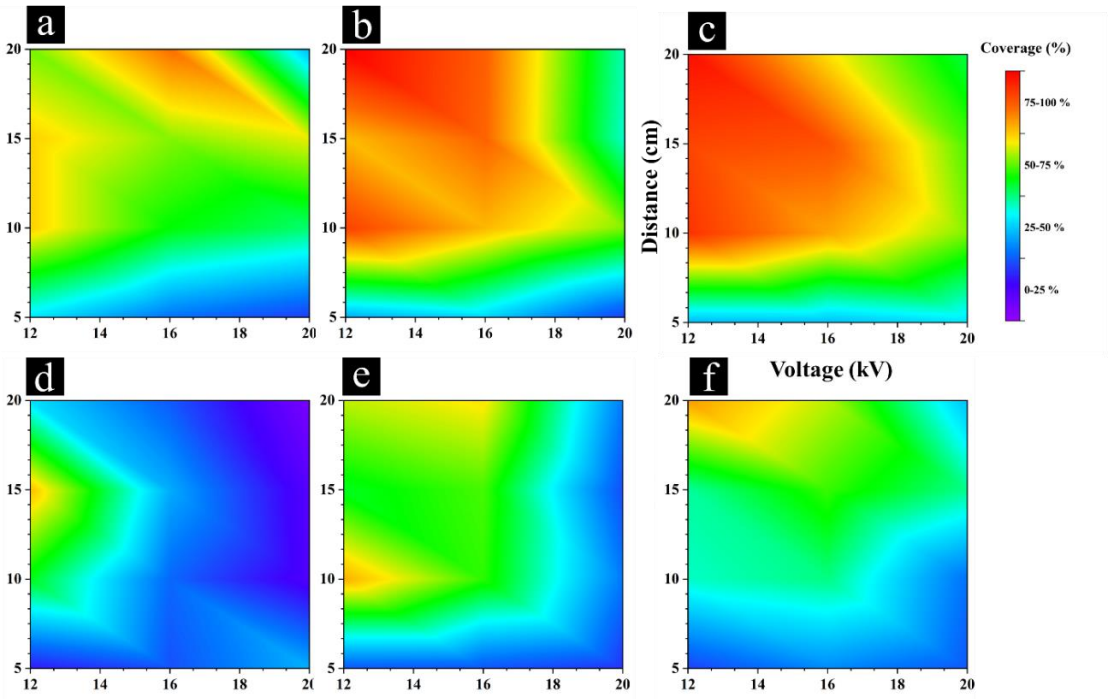

Figure 11. Comparison of the formation fibrous mat of PMMA with different conditions of constant concentration and flow rate. a) C=10 wt.% and F.R.=0.3 ml.h^{-1}, b) C=10 wt.% and F.R.=0.6 ml.h^{-1}, c) C=10 wt.% and F.R.=0.9 ml.h^{-1}, d) C=12.5 wt.% and F.R.=0.3 ml.h^{-1}, e) C=12.5 wt.% and F.R.=0.6 ml.h^{-1}, and f) C=12.5 wt.% and F.R.=0.9 ml.h^{-1}.

The electrospinning jet formation is visualized using a high-speed camera, as shown in Figure 12. Prior to applying the high voltage between the needle tip and collector, the syringe pump injected the solution, and the shape of the droplet was distorted toward the ground due to the gravity force (Figure 12a). The shape of the polymeric droplet, which emerges from the tip of the needle, is influenced by an electric field force and other forces such as inertia, hydrostatic pressure, and viscoelastic forces. By surpassing the electric field from the threshold point, the generated electrostatic charges on the droplet surface cause the elongation of the structure (so-called the Taylor cone). The forward electrostatic force and solution inertia overcome the backward viscous and downward gravity forces and form the jet (Figure 12b-c). However, due to the droplet's rapid acceleration toward the collector and thick cross-section of the generated

jet (Figure 12d), the gravity force dominates and makes the unstable jet bend and move in different paths (Figure 12e).

Meanwhile, the supplied amount of the solution is insufficient to provide enough material, and the Taylor cone becomes depleted (Figure 12e-f). The unstable jet stabilizes by establishing an balance between the applied forces (Figure 12g-i), and a continuous and stable electrospinning jet forms in 56 ms just after initiating the electrical field (Figure 12j-m). During the stabilization stage, the multi-jet mode is visible for a fraction of a second, and the formed jets repel each other due to their identical charges which is shown in Figure 12i.

The samples are shown in Figure 11, which were electrospun uniformly, were selected to investigate the morphology and diameter of the fibers, and their SEM images and diameter distribution are included along with the corresponding label numbers in Figure 13.

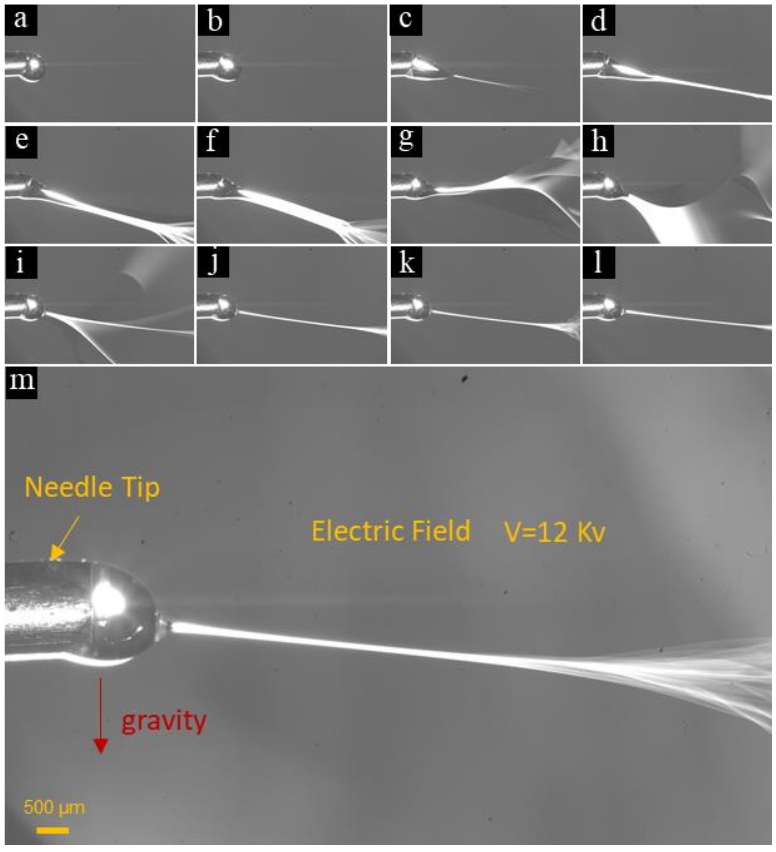

Figure 12. Formation of the Taylor cone with process parameters of V=12 Kv, flow rate= 0.6 ml.h-1, distance=20 cm, and composition= 10 wt.% PMMA in DMF. (a and b) before applying the electric field, (c) the high-voltage and electric field cause stretching of the droplet toward the collector, (d - j) the instability of jet because of the interactions of the charges on the electrified microjet, (k-m) a stable slim microjet formation. The time intervals of the images are 6667 µs.

It is reported in the literature that the composite electrospun nanofibers with small diameters exhibit better mechanical properties and are more favorable for functionalization purposes due to the higher surface-to-volume ratio of the mat. Furthermore, in every case, well-defined and well-controlled (mostly narrow range) diameter distributions meet the requirements for optimizing the parameters [59].

The polymeric solution feeding rate directly affects the electrospun fiber morphology and formation of the beads during the process. The first stage is generally related to the charge density of the liquid cone and stable jet formation. It is also linked with the evaporation of solvent from polymeric fibers. The effect of feeding rate on the fiber diameter distribution can be observed in Figure 13a-c, which displays that the size of fibers increases with the flow rate. Therefore, there should be a balance between the solution's feeding rate and the exiting material from the needle to obtain a continuous fiber with the smallest possible diameter.

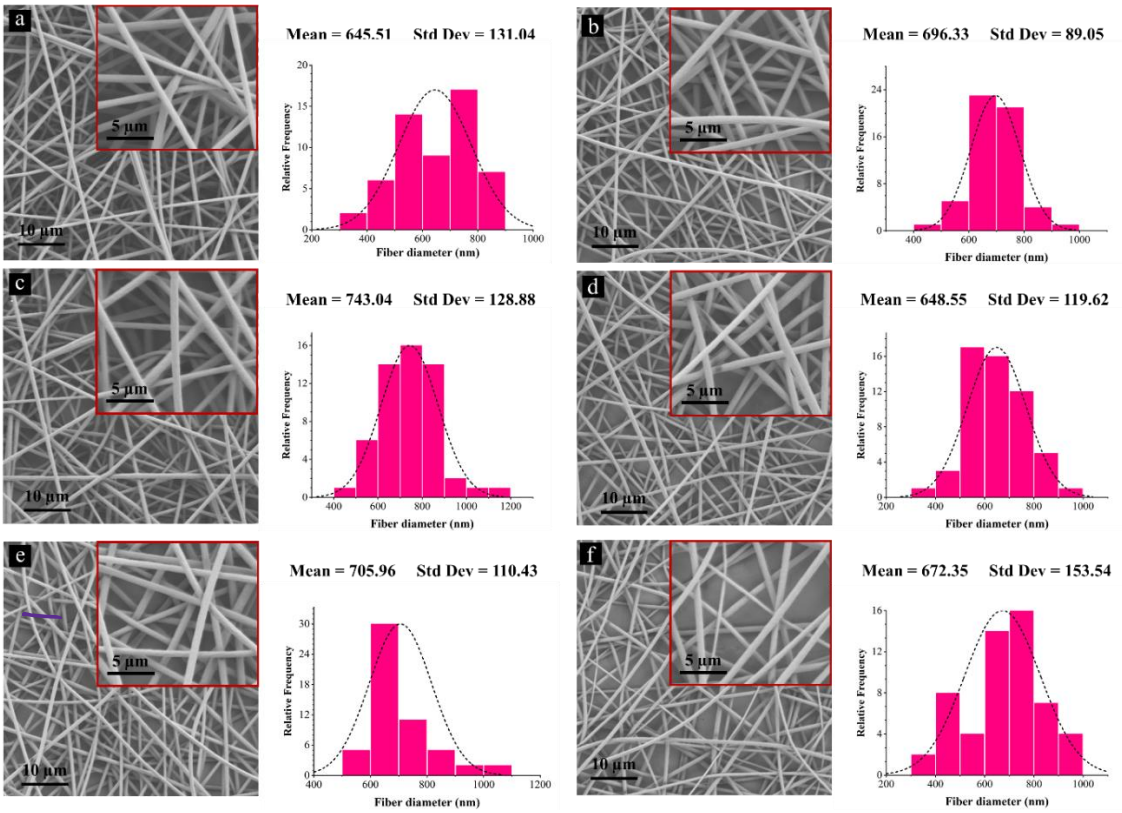

Figure 13. SEM images and fiber diameter size distribution of PMMA electrospun mats for different process parameters. a) V=12 Kv, F.R.= 0.3 ml.h^{-1}, and D=10 cm, b) V=12 Kv, F.R.= 0.6 ml.h^{-1}, and D=20 cm, c) V=12 Kv, F.R.= 0.9 ml.h^{-1}, and D=10 cm, d) V=12 Kv, F.R.= 0.9 ml.h^{-1}, and D=15 cm, e) V=12 Kv, F.R.= 0.9 ml.h^{-1}, and D=20 cm, and f) V=16 Kv, F.R.= 0.9 ml.h^{-1}, and D=15 cm.

The solvent's evaporation takes place between the needle and collector, and the optimum distance provides sufficient time for the solvent to evaporate before reaching the collector. Otherwise, the formation of the beads would be inevitable. The longer the distance is, the thinner the fibers are. Based on the results as mentioned earlier, the electrospinning condition for obtaining fibrous mat from 10 wt.% polymer/solvent solution with the fiber diameter of 696 nm and 100% surface coverage was optimized by applying the electric field of 12 kV, the flow rate of 0.6 $ml.h^{-1,}$ and the distance of 20 cm.

PEG was introduced to the solution as the second polymeric component. By considering 10 wt.% polymer/solvent ratio as the optimum one for fabricating fibers, three solutions with PEG concentrations of 20, 30, and 40 wt.% were electrospun, and the diameter of the obtained fibers are listed in Table 2. The mean fiber diameter decreases with the PEG concentration up to 30 wt.%. The polymeric solution viscosity decreases by adding the low molecular weight PEG, and beads formation can be observed by electrospinning 40 wt.% PEG solution. Moreover, the sufficient amount of the PEG does not interact with the PMMA solution to act as uniform compared to lower amounts.

Table 2. The average diameter of electrospun PMMA nanofibers with the addition of different amounts of PEG

Polymer Solution Composition	Nanofiber Diameter (nm)
PMMA (Optimized Condition)	696.33 ± 89.05
PMMA- 20 wt.% PEG	472.75 ± 84.64
PMMA- 30 wt.% PEG	462.31 ± 89.91
PMMA- 40 wt.% PEG	747.65 ± 145.27

The third component of the composite is the synthesized silica NPs in the IPA solution (Figure 14). The different ratios of the TEOS to ammonia are taken as the control parameter for synthesizing different sizes of silica nanoparticles. The concentration of the synthesizing baths and the average size of the achieved silica nanoparticles are included in Table 3.

Table 3. Concentration of the baths and the sizes of the synthesized silica nanoparticles

Batch number	$[TEOS]/[NH_3]_{aq}$	Mean Particle Size (nm)
1	4	102
2	4.8	97
3	6	86
4	8	74
5	12	65

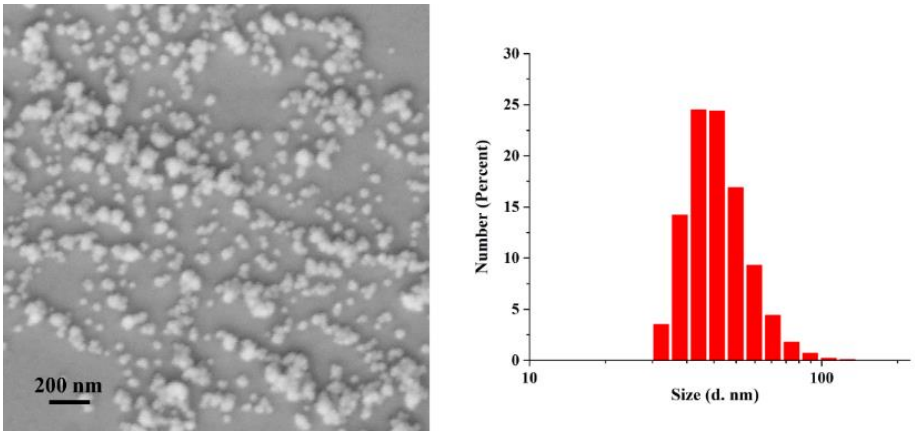

Figure 14. Synthesized SiO_2 NPs a) SEM image of the particles after drying from the solution and b) particle size distribution of silica NPs in the synthesized medium.

The third step of preparing a ternary electrospun composite is adding the silica nanoparticles to the PMMA-30 wt.% PEG electrospinning solution. Synthesized silica NPs in different solutions in five levels were added to the solution with mentioned mean sizes. The solutions for hybrid material electrospinning were prepared considering the concentrations in Table 4.

Table 4. Concentrations of different materials and ratio of used materials concerning each other.

parameter	value
PMMA: PEG	70:30
Polymer solid ratio	10 wt.%
Powder (SiO_2): Polymer	10:90
Solid (Polymer + SiO_2) Ratio	7.5 wt.%

The weights of silica NPs in each synthesized batch were different. Therefore, different solvent volumes (isopropyl alcohol) were used to prepare fixed concentration electrospinning solutions, as mentioned in Table 4. Since the ternary composite solution has different solvents, polymers, and other chemicals, the fabricated electrospun mats show different morphology, especially in the case of the formation of beads. The first stage is related to the change in viscosity and then is linked with their conductivity and dipole-moment, volatile nature of the solvents, and evaporation of the solvents during the flight of polymeric fibers.

Figure 15 shows the electrospun nanofibers with silica NPs on their surface for the optimum silica batch (batch number 5, Table 2). The optimum batch is achieved due to the lower alcohol amount, which transfers to the electrospinning solution from the synthesized silica batch. While silica NPs have an increasing effect on the viscosity, the inclusion of a second solvent (IPA) has an adverse effect. The balance between the counteracting effects results in batch 5, which leads to fewer beads in the electrospun mats.

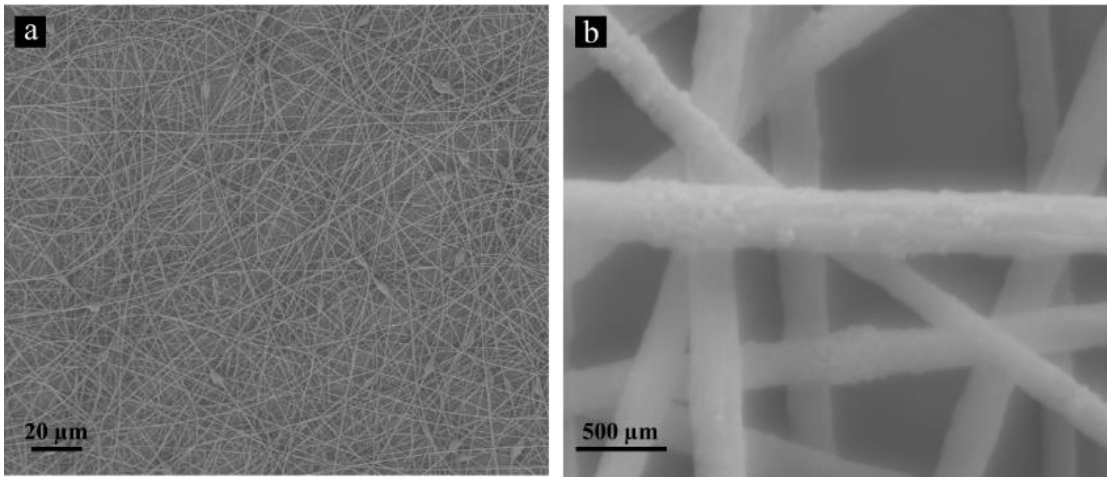

Figure 15. SEM images of PMMA- 30 wt.% PEG- SiO_2 electrospun mats. a) the broad microscopic view with some beads, and b) homogenous distribution of silica NPs ascertained on the surface of fibers.

3.2.2 PeakForce QNM

The nanoscale mechanical properties and surface of three samples of PMMA, PMMA-30wt.%PEG, and PMMA-30wt.%PEG-silica nanoparticles electrospun nanofibers are conducted. The height images and surface profile of the electrospun

nanofibers (Figure 16) show that the diameter of the fibers are in the range of 300 nm to 1μm, which are consistent with the SEM images. The root mean square (RMS) of the DMT modulus of PMMA, PMMA-30wt.%PEG-silica nanoparticles, and PMMA-30wt.%PEG electrospun nanofibers were 126, 402, 441 MPa respectively. The DMT modulus of PMMA-30wt.%PEG is the highest among the samples and these results are confirmed by tensile strength tests. Figure 17 shows PMMA-30wt.%PEG-silica nanoparticles electrospun nanofiber's height and DMT modulus profile. The AFM sample was prepared using scotch tape method by applying an adhesive tape to the electrospun nanofibers' mat and pulling it away and repeating the same procedure multiple times on the fresh adhesive tapes. The average DMT modulus of the electrospun fiber along its length was about 300 MPa. The observed picks on the DMT modulus diagram can be related to the silica nanoparticles, which are embedded in the structure of the fiber.

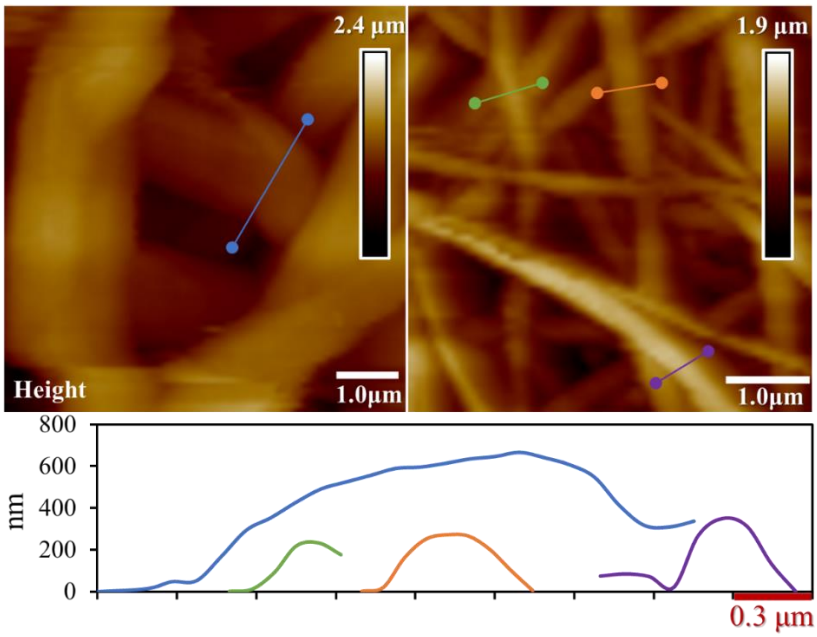

Figure 16. AFM Height images of PMMA electrospun nanofibers

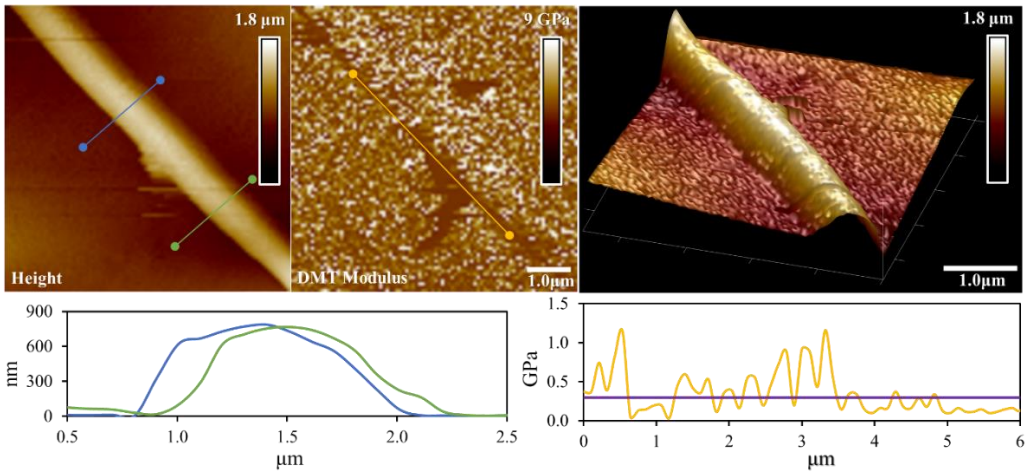

Figure 17. AFM height image, DMT modulus, and 3D height image of PMMA-30wt.%PEG-silica nanoparticles electrospun nanofiber

3.2.3 FTIR analysis

The FTIR analysis of the electrospun nanofibers is presented in Figure 18. The peak at 2949 cm^{-1} is related to the C–H stretching vibration, and the peak at 1726 cm^{-1} corresponds to acrylate carboxyl groups. The FTIR band at 1386 cm^{-1} is due to O–CH_3 bending vibrations, whereas the peak at 1241 cm^{-1} is related to the twisting mode of the –CH_2 group in PMMA. The FTIR peak of PMMA at 1435 cm^{-1} stands for the bending of C–H bonds in the –CH_3 group, and the strong peak at 1147 cm^{-1} is associated with the stretching vibration of the C–O bond in the C–O–C moiety as shown in Figure 18 [127,128]. For PEG, the 942–1092 cm^{-1} band originates from C–O ether groups stretching. The alkyl (R–CH_2) stretching modes at 2865 cm^{-1} can be observed, and the hydroxyl group contribution is observed at 3438 cm^{-1} [129]. The presence of SiO_2 can be confirmed with two main characteristic peaks at around 749 cm^{-1} and 1095 cm^{-1}, which correspond to Si-O bending vibration and asymmetric stretching vibration bands of the siloxane bonds (Si-O-Si), respectively. The band at around 3502 cm^{-1} is attributed to Si-OH, characteristics of the -OH group. The Si-OH band existence can be related to the absorbed water molecules from the environment by silica NPs [129].

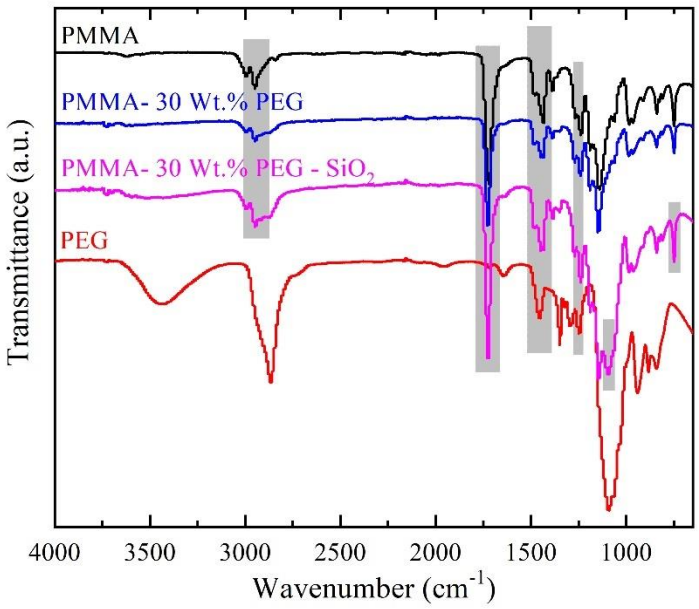

Figure 18. FTIR spectra of PMMA, PEG, PMMA- 30 wt.% PEG electrospun mat, and PMMA- 30 wt.% PEG -SiO_2 NPs electrospun mat.

3.2.4 Water contact angle

The water contact angle changes at 0, 5, and 10 seconds were measured to determine the effect of PEG content on the wettability of the PMMA-PEG electrospun (Figure 19). PMMA is an intrinsic hydrophobic polymer [70], and the highest contact angle among the samples (123.52°) corresponds to the PMMA electrospun mat. Consequently, it shows low fouling, and flux and hydrophilicity improvements can be achieved by the addition of PEG due to easily linking repeating units (CH_2-CH_2O) with water molecules via hydrogen bonding. As shown in Figure 19, the droplets start to diffuse inside the fibrous mats with different rates depending on the ratio of the blended polymer. The addition of the PEG up to 30 wt.% shows a decrease in water contact angle (t=0 s). However, in the PMMA- 40 wt.% PEG electrospun mat, an increase in water contact angle was observed. It seems that the solutions with a higher content of hydrophilic PEG lead to phase segregation of polymers and splashing PEG without any engagement in the morphology of fibrous electrospinning mats [130], which is in agreement with SEM images.

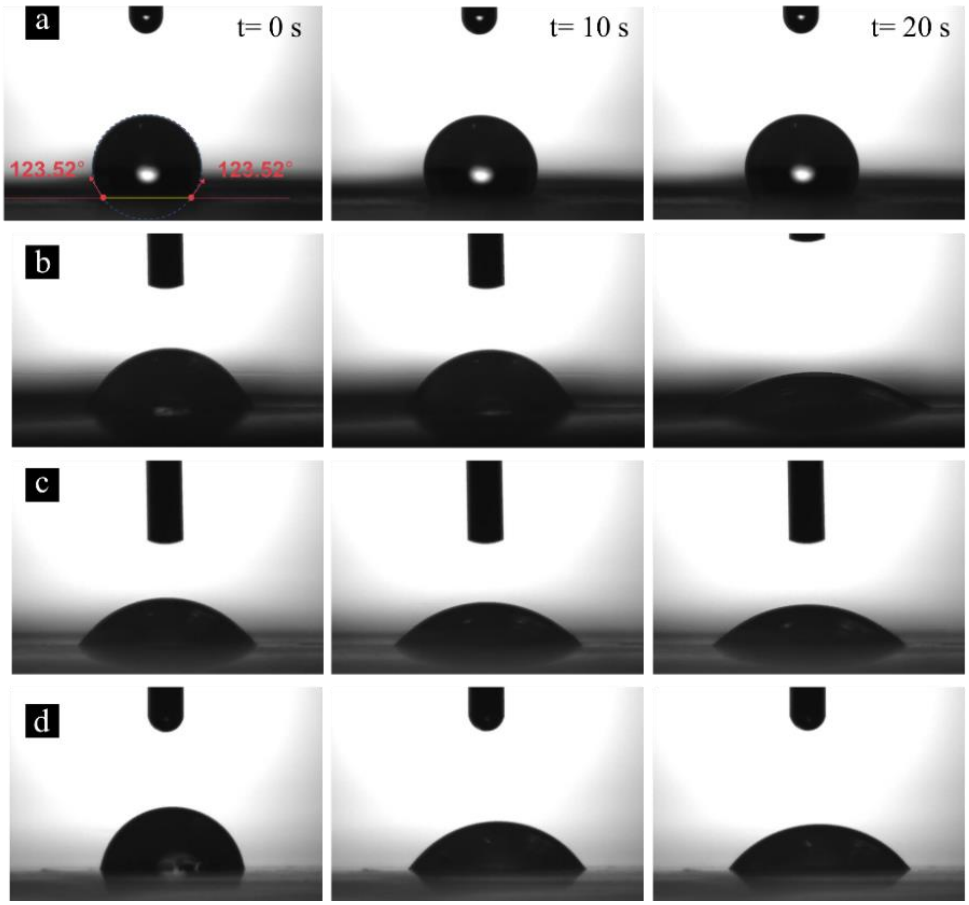

Figure 19. Contact angle for a) PMMA, b) PMMA - 20 wt.% PEG, c) PMMA - 30 wt.% PEG and d) PMMA - 40 wt.% PEG at the beginning of analysis and after 10 and 20 seconds.

3.2.5 Thermal stability

The thermal stability of the electrospun mats was analyzed with TGA. The characteristic TGA curves of PMMA-based electrospun mats and the weight changes as a function of temperature for different electrospun fibers are compared in Figure 20a. At the first stage, based on the hydrophobic properties of PMMA, just a tiny amount of weight loss can be seen at 0-100 °C. The second stage, between 250 and 300 °C, is related to the decomposition of PMMA unsaturated chain-ends. The third stage, above 300 °C (at around 365 °C), is attributed to the random scission of the polymeric chains [131]. The slight weight loss between room temperature to 100 °C, in Figure 20b and c, results from the elimination of adsorbed water due to the hydrophobic nature of PMMA components. The weight loss steps in b and c are different and have higher losses since PEG was added to electrospun mats. For the cases, which contain PEG, at around 200 °C, the ether bonds (CH_2–O–CH_2) break and form more stable bonds of methylene (CH_2) and therefore, small molecules are released. At the range of 250 to 400 °C also, there is a

degradation step for PEG and composite related to degradation and evaporation of the alcohol compounds (Figure 20b) [132,133]. After the addition of silica NPs, the peak in the range of 270-330 °C is attributable to the release of silanol-bonded water since the silanol-bonded water is stable and is eliminated at relatively higher temperatures (Figure 20c) [134]. At temperatures above 500 °C, the polymers decompose, and the entire polymer mass is burned. However, the embedded silica nanoparticles in the PMMA- 30 wt.% PEG- SiO_2 NPs do not decompose at temperatures above 500 ºC. These results also prove that silica nanoparticles form almost 8% of the weight of the fibers.

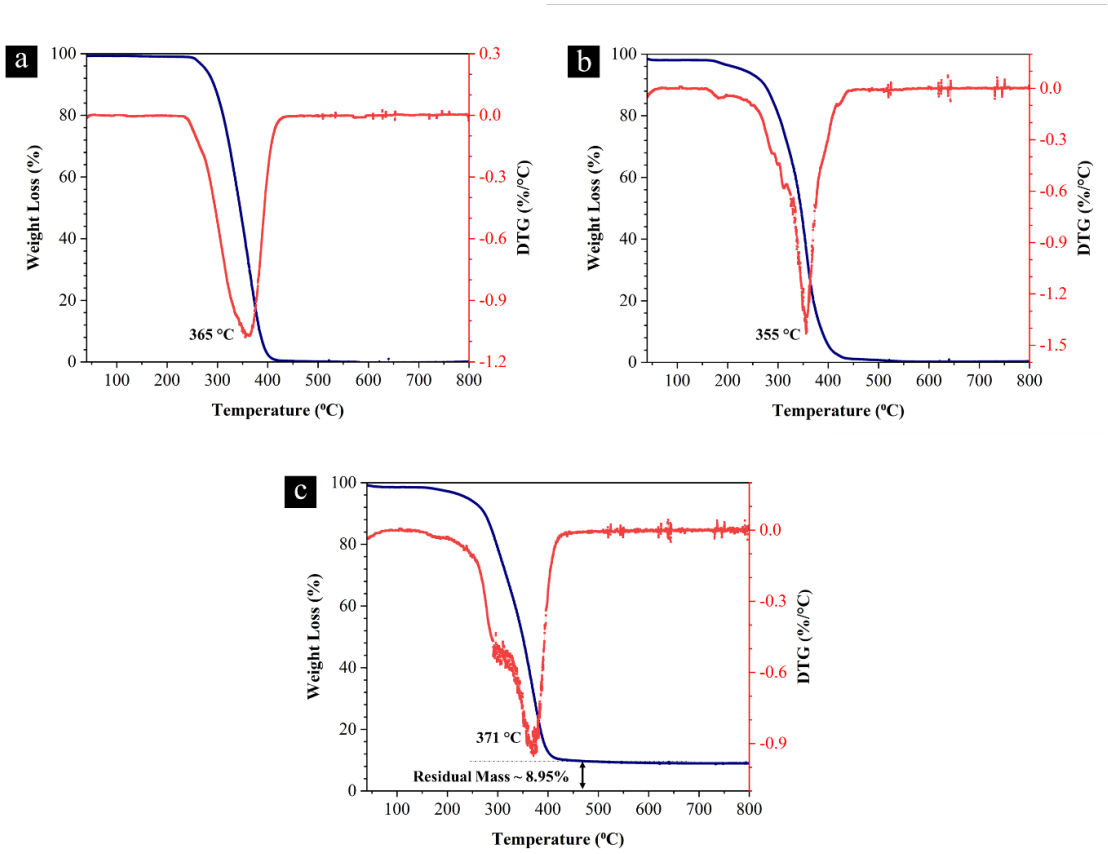

Figure 20. TGA diagram of a) PMMA, b) PMMA- 30 wt.% PEG, and c) PMMA- 30 wt.% PEG -SiO_2 NPs electrospun mat.

3.2.6 Mechanical Properties

For the applications such as filters and tissue engineering, the mechanical strength of electrospun mats is crucial for meeting the durability requirement. Therefore, the tensile tests were conducted to evaluate PMMA and PMMA-based composite electrospun nanofibers mechanical properties, and their stress-strain curves are given in Figure 21. The ultimate tensile stress and elongation at failure of the different electrospun mats are visible in this figure. The strength of polymeric materials can be improved with the

addition of rigid reinforcement into the soft polymeric matrix, but this is accompanied by a compromise in ductility [135]. The ultimate strength of the samples is obtained as 0.035, 0.35, and 0.12 MPa for PMMA, PMMA-30 wt.% PEG, and PMMA-30 wt.% PEG- SiO_2 NPs, respectively.

Although the introduction of silica nanoparticles to the fibers reduces the mechanical properties of PMMA-PEG polymers, the functionalization and surface treatment could be performed more effectively in the presence of silica NPs. It should be noted that the PMMA-30 wt.% PEG-silica nanoparticles have four times higher ultimate tensile strength in comparison with PMMA polymers.

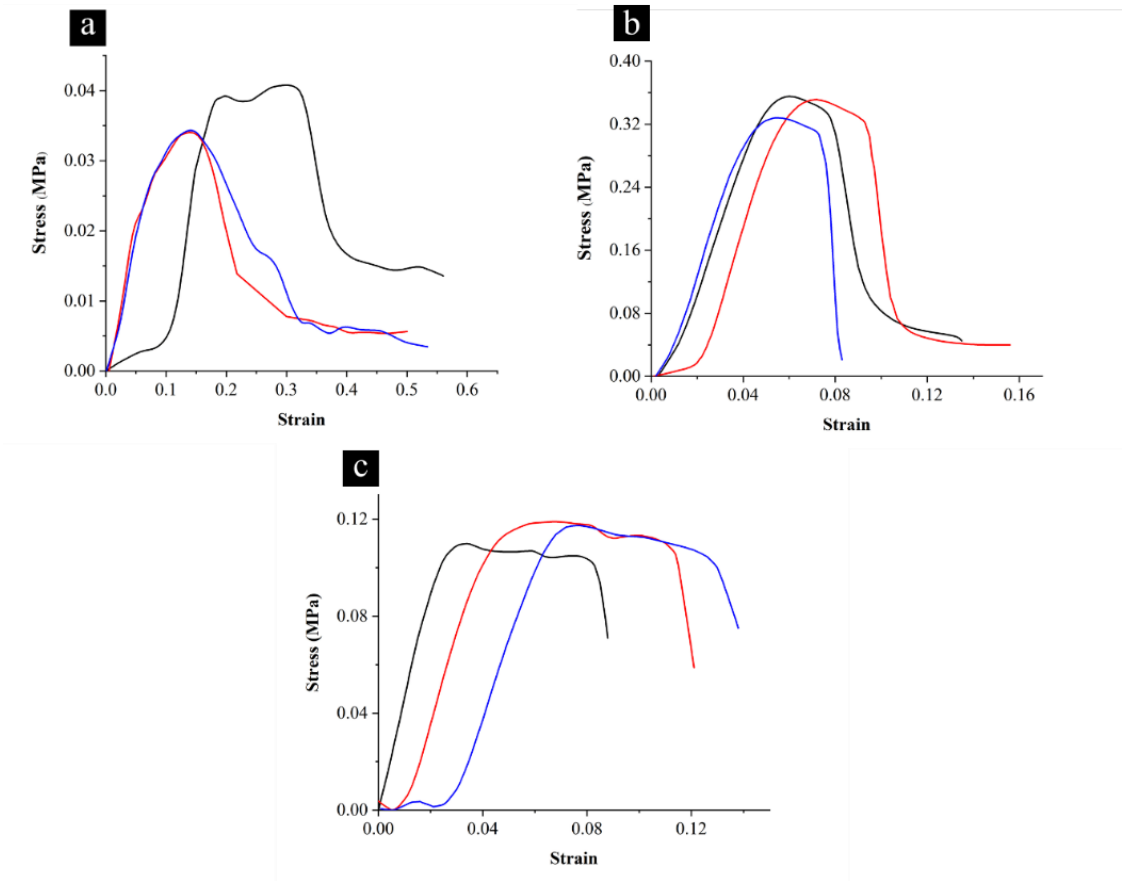

Figure 21. Stress-Strain curves of three different samples of a) PMMA b) PMMA-30 wt.% PEG and c) PMMA-30 Wt.% PEG- silica NPs.

Chapter 4. Conclusions and Future Works

4.1 Conclusion- Graphene Exfoliation Based on the "Hydrodynamic Cavitation on a Chip" Concept

In this thesis, first, the effects of the thermophysical properties of the working fluid (presence of graphite flakes) on cavitating flows were visualized and studied. Then, the impact of cavitating flows on graphite exfoliation was investigated. This method does not involve any surfactants or dispersion agents. According to the results, the suspensions with graphite flakes led to an increase in the number of the sites of heterogeneous bubble nucleation and to a decrease in the upstream pressure needed for cavitation inception and a developed cavitating flow pattern. Fragmentation of flakes and then exfoliation of layers was observed after exposures of 60-80 hydrodynamic cavitation cycles inside a microfluidic device and were rigorously characterized with different methods. With the implementation inside the reactor, it is possible to have a green, scalable, cost-effective, and energy-efficient process. The produced graphene nanosheets (lateral size ≥500 nm; thickness ~1.2 – 2.5 nm) meet the requirements well in many applications such as bioengineering, composites, and electronic devices. The results on hydrodynamic cavitation show a higher yield compared to the sonication and shear methods for graphene exfoliation.

4.2 Conclusion- Electrospinning of Ternary Composite of PMMA-PEG-SiO_2 Nanoparticles

In this thesis, a PMMA-based electrospun nanofibrous composite was fabricated. The PMMA and PEG 400 blended solution in DMF was mixed with silica NPs solution in IPA to obtain a hybrid fibrous mat. Process parameters such as the applied voltage, distance of the needle tip to the collector, flow rate of solution and solution concentration were investigated. Based on fiber formation and covering of the surface of the collector, and mean fibers diameter, which is extracted from SEM images, the optimum parameters, namely concentration of PMMA, applied voltage, flow rate, and distance between needle tip to the collector, were achieved at 10 wt.%, 12 kV, 0.6 $ml.h^{-1}$, and 20 cm, respectively. Moreover, the Taylor cone formation was monitored under optimum conditions. Then, the influence of PEG concentration on altering the mean diameter of the fibers, hydrophobicity of electrospun mats, thermal and mechanical properties were studied. The

results showed that blending and accordingly electrospinning of the PMMA solution with 30 wt.% PEG led to improvements in wettability of electrospun mat.

Furthermore, the fabricated electrospun mats with PMMA-30 wt.% PEG exhibited remarkable mechanical properties. The obtained ultimate strength was around ten times larger than the pure PMMA. Moreover, the fabricated ternary composite of PMMA-30 wt.% PEG-SiO_2 NPs led to three times enhancements in mechanical properties compared with PMMA, and the addition of silica NPs offers surface modification when needed in some applications such as filtration and bioengineering.

4.3 Future Works

• Based on the studies that we have had on exfoliation of graphite, it can be used for exfoliating other layered-materials by some modification in a microfluidic device and separate the layers of materials like Hexagonal Boron Nitride (hBN), which Turkey has an enormous source of this material, Transition Metal Dichalcogenides (TMDs) such as MoS_2, WS_2, and $MoSe_2$. or MXenes materials which are a hot topic in research bulletins.

The chemical aspect of different microfluidic devices can be studied with different chemicals such as Potassium Iodide (KI)

• Moreover, the produced graphene nanosheets with hydrodynamic cavitation method may implement water waste treatments as recyclable sources based on different aspects of HC reactors.

• For the electrospun mats, the next phase of works can be done based on interactions of fibers surfaces with bubbles/gases and water to separate gas phase and liquid. Furthermore, the SiO_2 NPs can host different modifications for a wide variety of applications in filtration and bioengineering.

Bibliography

[1] X. Wang, G. Shi, An introduction to the chemistry of graphene, Phys. Chem. Chem. Phys. 17 (2015) 28484–28504.

[2] P. Tiwari, V. Sharma, N. Kaur, K. Ahmad, S.M. Mobin, Sustainable Graphene Production: New Insights into Cannabis sativa Engineered Carbon Dots Based Exfoliating Agent for Facile Production of Graphene, ACS Sustain. Chem. Eng. 7 (2019) 11500–11510.

[3] L. Jiang, Z. Fan, Design of advanced porous graphene materials: From graphene nanomesh to 3D architectures, Nanoscale. 6 (2014) 1922–1945.

[4] S. Goenka, V. Sant, S. Sant, Graphene-based nanomaterials for drug delivery and tissue engineering, J. Control. Release. 173 (2014) 75–88.

[5] J. Liu, L. Cui, D. Losic, Graphene and graphene oxide as new nanocarriers for drug delivery applications, Acta Biomater. 9 (2013) 9243–9257.

[6] W.A. De Heer, C. Berger, E. Conrad, P. First, R. Murali, J. Meindl, Pionics: The emerging science and technology of graphene-based nanoelectronics, in: Tech. Dig. - Int. Electron Devices Meet. IEDM, 2007: pp. 199–202.

[7] S. Shintaro, Graphene for nanoelectronics, Jpn. J. Appl. Phys. 54 (2015) 040102 (1)-.040102 (12).

[8] H. Yang, L. Geng, Y. Zhang, G. Chang, Z. Zhang, X. Liu, M. Lei, Y. He, Graphene-templated synthesis of palladium nanoplates as novel electrocatalyst for direct methanol fuel cell, Appl. Surf. Sci. 466 (2019) 385–392.

[9] F. Sun, H. Tang, B. Zhang, X. Li, C. Yin, Z. Yue, L. Zhou, Y. Li, J. Shi, PEO-Linked MoS2-Graphene Nanocomposites with 2D Polar-Nonpolar Amphoteric Surfaces as Sulfur Hosts for High-Performance Li-S Batteries, ACS Sustain. Chem. Eng. 6 (2018) 974–982.

[10] B. Zhang, T. Cui, An ultrasensitive and low-cost graphene sensor based on layer-by-layer nano self-assembly, Appl. Phys. Lett. 98 (2011) 073116 (1)-073116 (3).

[11] H.J. Yoon, D.H. Jun, J.H. Yang, Z. Zhou, S.S. Yang, M.M.C. Cheng, Carbon dioxide gas sensor using a graphene sheet, Sensors Actuators, B Chem. 157 (2011) 310–313.

[12] M. Yankowitz, S. Chen, H. Polshyn, Y. Zhang, K. Watanabe, T. Taniguchi, D. Graf, A.F. Young, C.R. Dean, Tuning superconductivity in twisted bilayer graphene, Science (80-.). 363 (2019) 1059–1064.

[13] B. Zhang, P. Wei, Z. Zhou, T. Wei, Interactions of graphene with mammalian cells: Molecular mechanisms and biomedical insights, Adv. Drug Deliv. Rev. 105 (2016) 145–162.

[14] M. Coroş, F. Pogăcean, L. Măgeruşan, C. Socaci, S. Pruneanu, A brief overview on synthesis and applications of graphene and graphene-based nanomaterials, Front. Mater. Sci. 13 (2019) 23–32.

[15] S. Balasubramanyan, S. Sasidharan, R. Poovathinthodiyil, R.M. Ramakrishnan, B.N. Narayanan, Sucrose-mediated mechanical exfoliation of graphite: A green method for the large scale production of graphene and its application in catalytic reduction of 4-nitrophenol, New J. Chem. 41 (2017) 11969–11978.

[16] Y. Yao, Z. Lin, Z. Li, X. Song, K.S. Moon, C.P. Wong, Large-scale production of two-dimensional nanosheets, J. Mater. Chem. 22 (2012) 13494–13499.

[17] V. Bianchi, T. Carey, L. Viti, L. Li, E.H. Linfield, A.G. Davies, A. Tredicucci, D. Yoon, P.G. Karagiannidis, L. Lombardi, F. Tomarchio, A.C. Ferrari, F. Torrisi, M.S. Vitiello, Terahertz saturable absorbers from liquid phase exfoliation of graphite, Nat. Commun. 8 (2017) 1–9.

[18] Y.-Z. Wang, T. Chen, H.-H. Liu, X.-C. Wang, X.-X. Zhang, Direct Liquid Phase Exfoliation of Graphite to Produce Few-Layer Graphene by Microfluidization, J. Nanosci. Nanotechnol. 19 (2018) 2078–2086.
[19] B.H. Al-Tamimi, S.B.H. Farid, F.A. Chyad, Modified Unzipping Technique to Prepare Graphene Nano-Sheets, in: J. Phys. Conf. Ser., Institute of Physics Publishing, 2018, 12020 (1)-12020 (5).
[20] A.A. Silva, R.A. Pinheiro, A.C. Rodrigues, M.R. Baldan, V.J. Trava-Airoldi, E.J. Corat, Graphene sheets produced by carbon nanotubes unzipping and their performance as supercapacitor, Appl. Surf. Sci. 446 (2018) 201–208.
[21] M.S. Poorali, M.M. Bagheri-Mohagheghi, Synthesis and physical properties of multi-layered graphene sheets by Arc-discharge method with TiO2 and ZnO catalytic, J. Mater. Sci. Mater. Electron. 28 (2017) 6186–6193.
[22] D. V. Smovzh, I.A. Kostogrud, S.Z. Sakhapov, A. V. Zaikovskii, S.A. Novopashin, The synthesis of few-layered graphene by the arc discharge sputtering of a Si-C electrode, Carbon N. Y. 112 (2017) 97–102.
[23] J.I. Fujita, T. Hiyama, A. Hirukawa, T. Kondo, J. Nakamura, S.I. Ito, R. Araki, Y. Ito, M. Takeguchi, W.W. Pai, Near room temperature chemical vapor deposition of graphene with diluted methane and molten gallium catalyst, Sci. Rep. 7 (2017) 1–10.
[24] L. Lin, J. Zhang, H. Su, J. Li, L. Sun, Z. Wang, F. Xu, C. Liu, S. Lopatin, Y. Zhu, K. Jia, S. Chen, D. Rui, J. Sun, R. Xue, P. Gao, N. Kang, Y. Han, H.Q. Xu, Y. Cao, K.S. Novoselov, Z. Tian, B. Ren, H. Peng, Z. Liu, Towards super-clean graphene, Nat. Commun. 10 (2019) 1–7.
[25] J.D. Teeter, P.S. Costa, M. Mehdi Pour, D.P. Miller, E. Zurek, A. Enders, A. Sinitskii, Epitaxial growth of aligned atomically precise chevron graphene nanoribbons on Cu(111), Chem. Commun. 53 (2017) 8463–8466.
[26] H. Zhang, F. Ding, H. Li, F. Qu, H. Meng, H. Gu, Controlled synthesis of monolayer graphene with a high quality by pyrolysis of silicon carbide, Mater. Lett. 244 (2019) 171–174.
[27] T.P. Teng, S.C. Chang, Z.Y. Chen, C.K. Huang, S.F. Tseng, C.R. Yang, High-yield production of graphene flakes using a novel electrochemical/mechanical hybrid exfoliation, Int. J. Adv. Manuf. Technol. 104 (2019) 2751–2760.
[28] E. Gao, S.Z. Lin, Z. Qin, M.J. Buehler, X.Q. Feng, Z. Xu, Mechanical exfoliation of two-dimensional materials, J. Mech. Phys. Solids. 115 (2018) 248–262.
[29] K.B. Ricardo, A. Sendecki, H. Liu, Surfactant-free exfoliation of graphite in aqueous solutions, Chem. Commun. 50 (2014) 2751–2754.
[30] T. Hui, D.H. Adamson, Kinetic study of surfactant-free graphene exfoliation at a solvent interface, Carbon N. Y. 168 (2020) 354–361.
[31] Y. Hernandez, V. Nicolosi, M. Lotya, F.M. Blighe, Z. Sun, S. De, I.T. McGovern, B. Holland, M. Byrne, Y.K. Gun'ko, J.J. Boland, P. Niraj, G. Duesberg, S. Krishnamurthy, R. Goodhue, J. Hutchison, V. Scardaci, A.C. Ferrari, J.N. Coleman, High-yield production of graphene by liquid-phase exfoliation of graphite, Nat. Nanotechnol. 3 (2008) 563–568.
[32] M. Yi, Z. Shen, A review on mechanical exfoliation for the scalable production of graphene, J. Mater. Chem. A. 3 (2015) 11700–11715.
[33] M. Quintana, J.I. Tapia, M. Prato, Liquid-phase exfoliated graphene: functionalization, characterization, and applications, Beilstein J. Nanotechnol. 5 (2014) 2328–2338.
[34] M.T. Gevari, A.H. Shafaghi, L.G. Villanueva, M. Ghorbani, A. Koşar, Engineered Lateral Roughness Element Implementation and Working Fluid Alteration to

Intensify Hydrodynamic Cavitating Flows on a Chip for Energy Harvesting, Micromachines. 11 (2019) 1-16.
[35] A.J. Jadhav, C.R. Holkar, A.D. Goswami, A.B. Pandit, D. V. Pinjari, Acoustic Cavitation as a Novel Approach for Extraction of Oil from Waste Date Seeds, ACS Sustain. Chem. Eng. 4 (2016) 4256–4263.
[36] V. Štengl, Preparation of Graphene by Using an Intense Cavitation Field in a Pressurized Ultrasonic Reactor, Chem. - A Eur. J. 18 (2012) 14047–14054.
[37] M.T. Gevari, M. Ghorbani, A.J. Svagan, D. Grishenkov, A. Kosar, Energy harvesting with micro scale hydrodynamic cavitation-thermoelectric generation coupling, AIP Adv. 9 (2019) 105012 (1)-105012 (11).
[38] X.J. Lee, B.Y.Z. Hiew, K.C. Lai, L.Y. Lee, S. Gan, S. Thangalazhy-Gopakumar, S. Rigby, Review on graphene and its derivatives: Synthesis methods and potential industrial implementation, J. Taiwan Inst. Chem. Eng. 98 (2019) 163–180.
[39] M.I. Kairi, S. Dayou, N.I. Kairi, S.A. Bakar, B. Vigolo, A.R. Mohamed, Toward high production of graphene flakes-a review on recent developments in their synthesis methods and scalability, J. Mater. Chem. A. 6 (2018) 15010–15026.
[40] M. Li, A. Bussonnière, M. Bronson, Z. Xu, Q. Liu, Study of Venturi tube geometry on the hydrodynamic cavitation for the generation of microbubbles, Miner. Eng. 132 (2019) 268–274.
[41] M.T. Gevari, T. Abbasiasl, S. Niazi, M. Ghorbani, A. Koşar, Direct and indirect thermal applications of hydrodynamic and acoustic cavitation: A review, Appl. Therm. Eng. 171 (2020) 115065 (1)- 115065 (29).
[42] A. Nayebzadeh, H. Tabkhi, Y. Peles, Hydrodynamic Cavitation Downstream a Micropillar Entrained Inside a Microchannel - A Parametric Study, J. Fluids Eng. Trans. ASME. 141 (2019) 011101(1)-011101(13).
[43] Z. Jin, Z. Gao, X. Li, J. Qian, Cavitating Flow through a Micro-Orifice, Micromachines. 10 (2019) 191.
[44] L. Liu, Z. Shen, S. Liang, M. Yi, X. Zhang, S. Ma, Graphene for reducing bubble defects and enhancing mechanical properties of graphene/cellulose acetate composite films, J. Mater. Sci. 49 (2014) 321–328.
[45] X. Qiu, V. Bouchiat, D. Colombet, F. Ayela, Liquid-phase exfoliation of graphite into graphene nanosheets in a hydrocavitating “lab-on-a-chip,” RSC Adv. 9 (2019) 3232–3238.
[46] M. Yi, Z. Shen, J. Zhu, A fluid dynamics route for producing graphene and its analogues, Chinese Sci. Bull. 59 (2014) 1794–1799.
[47] S. Ribeiro, T. Ribeiro, C. Ribeiro, D. Correia, J. Farinha, A. Gomes, C. Baleizão, S. Lanceros-Méndez, Multifunctional Platform Based on Electroactive Polymers and Silica Nanoparticles for Tissue Engineering Applications, Nanomaterials. 8 (2018) 933.
[48] J. Yoon, H.S. Yang, B.S. Lee, W.R. Yu, Recent Progress in Coaxial Electrospinning: New Parameters, Various Structures, and Wide Applications, Adv. Mater. 30 (2018) 1704765 (1)-1704765 (23).
[49] X.X. He, J. Zheng, G.F. Yu, M.H. You, M. Yu, X. Ning, Y.Z. Long, Near-Field Electrospinning: Progress and Applications, J. Phys. Chem. C. 121 (2017) 8663–8678.
[50] F.E. Ahmed, B.S. Lalia, R. Hashaikeh, A review on electrospinning for membrane fabrication: Challenges and applications, Desalination. 356 (2015) 15–30.
[51] A.C. Mendes, K. Stephansen, I.S. Chronakis, Electrospinning of food proteins and polysaccharides, Food Hydrocoll. 68 (2017) 53–68.
[52] J. Xue, T. Wu, Y. Dai, Y. Xia, Electrospinning and electrospun nanofibers:

Methods, materials, and applications, Chem. Rev. 119 (2019) 5298–5415.
[53] A. Haider, S. Haider, I.K. Kang, A comprehensive review summarizing the effect of electrospinning parameters and potential applications of nanofibers in biomedical and biotechnology, Arab. J. Chem. 11 (2018) 1165–1188.
[54] M.S. Islam, B.C. Ang, A. Andriyana, A.M. Afifi, A review on fabrication of nanofibers via electrospinning and their applications, SN Appl. Sci. 1 (2019) 1–16.
[55] C. Huang, N.L. Thomas, Fabrication of porous fibers via electrospinning: strategies and applications, Polym. Rev. 60 (2020) 595–647.
[56] J. Lasprilla-Botero, M. Álvarez-Láinez, J.M. Lagaron, The influence of electrospinning parameters and solvent selection on the morphology and diameter of polyimide nanofibers, Mater. Today Commun. 14 (2018) 1–9.
[57] F. Yalcinkaya, B. Yalcinkaya, O. Jirsak, Influence of salts on electrospinning of aqueous and nonaqueous polymer solutions, J. Nanomater. (2015) 134251(1)-134251(12).
[58] M. Putti, M. Simonet, R. Solberg, G.W.M. Peters, Electrospinning poly(ε-caprolactone) under controlled environmental conditions: Influence on fiber morphology and orientation, Polymer (Guildf). 63 (2015) 189–195.
[59] R. Stepanyan, A. V. Subbotin, L. Cuperus, P. Boonen, M. Dorschu, F. Oosterlinck, M.J.H. Bulters, Nanofiber diameter in electrospinning of polymer solutions: Model and experiment, Polymer (Guildf). 97 (2016) 428–439.
[60] Q. Liu, J. Zhu, L. Zhang, Y. Qiu, Recent advances in energy materials by electrospinning, Renew. Sustain. Energy Rev. 81 (2018) 1825–1858.
[61] Q. Wang, D.G. Yu, L.L. Zhang, X.K. Liu, Y.C. Deng, M. Zhao, Electrospun hypromellose-based hydrophilic composites for rapid dissolution of poorly water-soluble drug, Carbohydr. Polym. 174 (2017) 617–625.
[62] M. Makaremi, R.T. De Silva, P. Pasbakhsh, Electrospun nanofibrous membranes of polyacrylonitrile/halloysite with superior water filtration ability, J. Phys. Chem. C. 119 (2015) 7949–7958.
[63] A.W. Lee, C.C. Hsu, C.J. Chang, C.H. Lu, J.K. Chen, Preparation of biofiltration membranes by coating electrospun polyacrylonitrile fiber membranes with layer-by-layer supermolecular polyelectrolyte films, Colloids Surfaces B Biointerfaces. 190 (2020) 110953(1)-110953(10).
[64] T. Wu, M. Ding, C. Shi, Y. Qiao, P. Wang, R. Qiao, X. Wang, J. Zhong, Resorbable polymer electrospun nanofibers: History, shapes and application for tissue engineering, Chinese Chem. Lett. 31 (2020) 617–625.
[65] S. Ranganathan, K. Balagangadharan, N. Selvamurugan, Chitosan and gelatin-based electrospun fibers for bone tissue engineering, Int. J. Biol. Macromol. 133 (2019) 354–364.
[66] M.C. Li, S. Tong, J.T. Lin, K.Y.A. Lin, Y.F. Lin, Electrospun Co_3O_4 nanofiber as an efficient heterogeneous catalyst for activating peroxymonosulfate in water, J. Taiwan Inst. Chem. Eng. 106 (2020) 110–117.
[67] S. Ulrich, S.O. Moura, Y. Diaz, M. Clerc, A.G. Guex, J.R. de Alaniz, A. Martins, N.M. Neves, M. Rottmar, R.M. Rossi, G. Fortunato, L.F. Boesel, Electrospun colourimetric sensors for detecting volatile amines, Sensors Actuators, B Chem. 322 (2020) 128570(1)-128570(10).
[68] L. Wang, Z. Wang, Y. Sun, X. Liang, H. Xiang, Sb_2O_3 modified PVDF-CTFE electrospun fibrous membrane as a safe lithium-ion battery separator, J. Memb. Sci. 572 (2019) 512–519.
[69] X. Zheng, Y. Zheng, H. Zhang, Q. Yang, C. Xiong, Flexible MoS_2@electrospun

PVDF hybrid membrane as advanced anode for lithium storage, Chem. Eng. J. 370 (2019) 547–555.
[70] Z. Liu, J.H. Zhao, P. Liu, J.H. He, Tunable surface morphology of electrospun PMMA fiber using binary solvent, Appl. Surf. Sci. 364 (2016) 516–521.
[71] H.R. Munj, M.T. Nelson, P.S. Karandikar, J.J. Lannutti, D.L. Tomasko, Biocompatible electrospun polymer blends for biomedical applications, J. Biomed. Mater. Res. Part B Appl. Biomater. 102 (2014) 1517–1527.
[72] S. Piperno, L. Lozzi, R. Rastelli, M. Passacantando, S. Santucci, PMMA nanofibers production by electrospinning, Appl. Surf. Sci. 252 (2006) 5583–5586.
[73] X. Ni, W. Cheng, S. Huan, D. Wang, G. Han, Electrospun cellulose nanocrystals/poly(methyl methacrylate) composite nanofibers: Morphology, thermal and mechanical properties, Carbohydr. Polym. 206 (2019) 29–37.
[74] Z. Li, T. Li, L. An, P. Fu, C. Gao, Z. Zhang, Highly efficient chromium(VI) adsorption with nanofibrous filter paper prepared through electrospinning chitosan/polymethylmethacrylate composite, Carbohydr. Polym. 137 (2016) 119–126.
[75] Q. Fu, G. Lin, X. Chen, Z. Yu, R. Yang, M. Li, X. Zeng, J. Chen, Mechanically Reinforced PVdF/PMMA/SiO_2 Composite Membrane and Its Electrochemical Properties as a Separator in Lithium-Ion Batteries, Energy Technol. 6 (2018) 144–152.
[76] T.E. Newsome, S. V. Olesik, Electrospinning silica/polyvinylpyrrolidone composite nanofibers, J. Appl. Polym. Sci. 131 (2014) 40966(1)- 40966(9).
[77] G. Moradi, S. Zinadini, L. Rajabi, S. Dadari, Fabrication of high flux and antifouling mixed matrix fumarate-alumoxane/PAN membranes via electrospinning for application in membrane bioreactors, Appl. Surf. Sci. 427 (2018) 830–842.
[78] M.S. Islam, J.R. McCutcheon, M.S. Rahaman, A high flux polyvinyl acetate-coated electrospun nylon 6/SiO_2 composite microfiltration membrane for the separation of oil-in-water emulsion with improved antifouling performance, J. Memb. Sci. 537 (2017) 297–309.
[79] R.S. Kurusu, N.R. Demarquette, Surface properties evolution in electrospun polymer blends by segregation of hydrophilic or amphiphilic molecules, Eur. Polym. J. 89 (2017) 129–137.
[80] F. Sun, J. Guo, Y. Liu, Y. Yu, Preparation, characterizations and properties of sodium alginate grafted acrylonitrile/polyethylene glycol electrospun nanofibers, Int. J. Biol. Macromol. 137 (2019) 420–425.
[81] M.J. Park, R.R. Gonzales, A. Abdel-Wahab, S. Phuntsho, H.K. Shon, Hydrophilic polyvinyl alcohol coating on hydrophobic electrospun nanofiber membrane for high performance thin film composite forward osmosis membrane, Desalination. 426 (2018) 50–59.
[82] E. Hendrick, M. Frey, Increasing Surface Hydrophilicity in Poly(Lactic Acid) Electrospun Fibers by Addition of Pla-b-Peg Co-Polymers, J. Eng. Fiber. Fabr. 9 (2014) 153-164.
[83] L.C. Lins, F. Wianny, S. Livi, I.A. Hidalgo, C. Dehay, J. Duchet-Rumeau, J.F. Gérard, Development of Bioresorbable Hydrophilic-Hydrophobic Electrospun Scaffolds for Neural Tissue Engineering, Biomacromolecules. 17 (2016) 3172–3187.
[84] H.L. Tan, D. Kai, P. Pasbakhsh, S.Y. Teow, Y.Y. Lim, J. Pushpamalar, Electrospun cellulose acetate butyrate/polyethylene glycol (CAB/PEG) composite nanofibers: A potential scaffold for tissue engineering, Colloids Surfaces B

Biointerfaces. 188 (2020) 110713(1)-110713(8).
[85] S. Kiani, S.M. Mousavi, N. Shahtahmassebi, E. Saljoughi, Hydrophilicity improvement in polyphenylsulfone nanofibrous filtration membranes through addition of polyethylene glycol, Appl. Surf. Sci. 359 (2015) 252–258.
[86] C. Kuchi, G.S. Harish, P.S. Reddy, Effect of polymer concentration, needle diameter and annealing temperature on TiO_2-PVP composite nanofibers synthesized by electrospinning technique, Ceram. Int. 44 (2018) 5266–5272.
[87] Z.Q. Dong, X.H. Ma, Z.L. Xu, Z.Y. Gu, Superhydrophobic modification of PVDF-SiO2 electrospun nanofiber membranes for vacuum membrane distillation, RSC Adv. 5 (2015) 67962–67970.
[88] Z. Zhang, W. Zhang, M. Chen, Y. Jiang, R. Tian, J. Zhang, R. Fan, Fabrication of Co/Al_2O_3 Composite Nanofiber via Electrospinning with Tunable Magnetic Properties, Fibers Polym. 21 (2020) 2485–2493.
[89] R. Sigwadi, T. Mokrani, S. Dhlamini, P.F. Msomi, Nafion® reinforced with polyacrylonitrile/ZrO_2 nanofibers for direct methanol fuel cell application, J. Appl. Polym. Sci. 138 (2021) 49978(1)- 49978(8).
[90] Y. Hou, L. Cheng, Y. Zhang, X. Du, Y. Zhao, Z. Yang, High temperature electromagnetic interference shielding of lightweight and flexible ZrC/SiC nanofiber mats, Chem. Eng. J. 404 (2021) 126521(1)-126521(8).
[91] Y. Zhmayev, G.L. Shebert, S. Pinge, P. Kaur, H. Liu, Y.L. Joo, Non-enthalpic enhancement of spatial distribution and orientation of CNTs and GNRs in polymer nanofibers, Polymer (Guildf). 178 (2019) 121551(1)-121551(7).
[92] E. Ceretti, P.S. Ginestra, M. Ghazinejad, A. Fiorentino, M. Madou, Electrospinning and characterization of polymer–graphene powder scaffolds, CIRP Ann. - Manuf. Technol. 66 (2017) 233–236.
[93] J. Seyfi, I. Hejazi, S.H. Jafari, H.A. Khonakdar, F. Simon, Enhanced hydrophobicity of polyurethane via non-solvent induced surface aggregation of silica nanoparticles, J. Colloid Interface Sci. 478 (2016) 117–126.
[94] P. He, H.R. Cheng, Y. Le, J.F. Chen, Preparation and characterization of nano-sized Sr0.7Ca0.3TiO3 crystallines by low temperature aqueous synthesis method, Mater. Lett. 62 (2008) 2157–2160.
[95] S. Sriram, A. Kumar, Separation of oil-water via porous PMMA/SiO_2 nanoparticles superhydrophobic surface, Colloids Surfaces A Physicochem. Eng. Asp. 563 (2019) 271–279.
[96] W. Qing, X. Li, Y. Wu, S. Shao, H. Guo, Z. Yao, Y. Chen, W. Zhang, C.Y. Tang, In situ silica growth for superhydrophilic-underwater superoleophobic Silica/PVA nanofibrous membrane for gravity-driven oil-in-water emulsion separation, J. Memb. Sci. 612 (2020) 118476(1)-118476(8).
[97] Y. Chen, Z. Zhang, J. Yu, Z.-X. Guo, Poly(methyl methacrylate)/silica nanocomposite fibers by electrospinning, J. Polym. Sci. Part B Polym. Phys. 47 (2009) 1211–1218.
[98] Y. Chen, S. Liu, Z. Hou, P. Ma, D. Yang, C. Li, J. Lin, Multifunctional electrospinning composite fibers for orthotopic cancer treatment in vivo, Nano Res. 8 (2015) 1917–1931.
[99] X. Yang, Y. Pu, Y. Zhang, X. Liu, J. Li, D. Yuan, X. Ning, Multifunctional composite membrane based on $BaTiO_3$@PU/PSA nanofibers for high-efficiency PM2.5 removal, J. Hazard. Mater. 391 (2020) 122254(1)-122254(11).
[100] J. Zhang, H. Lu, C. Yan, Z. Yang, G. Zhu, J. Gao, F. Yin, C. Wang, Fabrication of conductive graphene oxide-WO_3 composite nanofibers by electrospinning and their enhanced acetone gas sensing properties, Sensors Actuators, B Chem. 264

(2018) 128–138.
[101] M. Ghorbani, A.K. Sadaghiani, L.G. Villanueva, A. Koşar, Hydrodynamic cavitation in microfluidic devices with roughened surfaces, J. Micromechanics Microengineering. 28 (2018) 075016.
[102] M. Ghorbani, G. Deprem, E. Ozdemir, A.R. Motezakker, L.G. Villanueva, A. Kosar, On "Cavitation on Chip" in Microfluidic Devices with Surface and Sidewall Roughness Elements, J. Microelectromechanical Syst. 28 (2019) 890–899.
[103] S.A. Hodge, M.K. Bayazit, K.S. Coleman, M.S.P. Shaffer, Unweaving the rainbow: A review of the relationship between single-walled carbon nanotube molecular structures and their chemical reactivity, Chem. Soc. Rev. 41 (2012) 4409–4429.
[104] M.K. Bayazit, K.S. Coleman, Probing the Selectivity of Azomethine Imine Cycloaddition to Single-Walled Carbon Nanotubes by Resonance Raman Spectroscopy, Chem. - An Asian J. 7 (2012) 2925–2930.
[105] C.J. Shih, A. Vijayaraghavan, R. Krishnan, R. Sharma, J.H. Han, M.H. Ham, Z. Jin, S. Lin, G.L.C. Paulus, N.F. Reuel, Q.H. Wang, D. Blankschtein, M.S. Strano, Bi- and trilayer graphene solutions, Nat. Nanotechnol. 6 (2011) 439-445.
[106] A.C. Ferrari, D.M. Basko, Raman spectroscopy as a versatile tool for studying the properties of graphene, Nat. Nanotechnol. 8 (2013) 235-246.
[107] L. Liu, Z. Shen, S. Liang, M. Yi, X. Zhang, S. Ma, Graphene for reducing bubble defects and enhancing mechanical properties of graphene/cellulose acetate composite films, J. Mater. Sci. 49 (2014) 321–328.
[108] J.M. Englert, C. Dotzer, G. Yang, M. Schmid, C. Papp, J.M. Gottfried, H.P. Steinrück, E. Spiecker, F. Hauke, A. Hirsch, Covalent bulk functionalization of graphene, Nat. Chem. 3 (2011) 279-286.
[109] M.K. Bayazit, In situ single-step reduction of bromine-intercalated graphite to covalently brominated and alkylated/brominated graphene, J. Mater. Res. 35 (2020) 1472-1480.
[110] J. Bin Wu, M.L. Lin, X. Cong, H.N. Liu, P.H. Tan, Raman spectroscopy of graphene-based materials and its applications in related devices, Chem. Soc. Rev. 47 (2018) 1822–1873.
[111] Z. Lin, P.S. Karthik, M. Hada, T. Nishikawa, Y. Hayashi, Simple Technique of Exfoliation and Dispersion of Multilayer Graphene from Natural Graphite by Ozone-Assisted Sonication, Nanomaterials. 7 (2017) 125(1)-125(10).
[112] Z. Shen, J. Li, M. Yi, X. Zhang, S. Ma, Preparation of graphene by jet cavitation, Nanotechnology. 22 (2011) 365306(1)-365306(8).
[113] A. Eckmann, A. Felten, A. Mishchenko, L. Britnell, R. Krupke, K.S. Novoselov, C. Casiraghi, Probing the nature of defects in graphene by Raman spectroscopy, Nano Lett. 12 (2012) 3925-3930.
[114] W. Liu, V.A. Tanna, B.M. Yavitt, C. Dimitrakopoulos, H.H. Winter, Fast Production of High-Quality Graphene via Sequential Liquid Exfoliation, ACS Appl. Mater. Interfaces. 7 (2015) 27027–27030.
[115] U. Khan, A. O'Neill, M. Lotya, S. De, J.N. Coleman, High-concentration solvent exfoliation of graphene, Small. 6 (2010) 864–871.
[116] P.G. Karagiannidis, S.A. Hodge, L. Lombardi, F. Tomarchio, N. Decorde, S. Milana, I. Goykhman, Y. Su, S. V. Mesite, D.N. Johnstone, R.K. Leary, P.A. Midgley, N.M. Pugno, F. Torrisi, A.C. Ferrari, Microfluidization of Graphite and Formulation of Graphene-Based Conductive Inks, ACS Nano. 11 (2017) 2742–2755.
[117] K.R. Paton, E. Varrla, C. Backes, R.J. Smith, U. Khan, A. O'Neill, C. Boland, M.

Lotya, O.M. Istrate, P. King, T. Higgins, S. Barwich, P. May, P. Puczkarski, I. Ahmed, M. Moebius, H. Pettersson, E. Long, J. Coelho, S.E. O'Brien, E.K. McGuire, B.M. Sanchez, G.S. Duesberg, N. McEvoy, T.J. Pennycook, C. Downing, A. Crossley, V. Nicolosi, J.N. Coleman, Scalable production of large quantities of defect-free few-layer graphene by shear exfoliation in liquids, Nat. Mater. 13 (2014) 624–630.

[118] Y. Xu, H. Cao, Y. Xue, B. Li, W. Cai, Liquid-phase exfoliation of graphene: An overview on exfoliation media, techniques, and challenges, Nanomaterials. 8 (2018) 942(1)-942(32).

[119] M. Lotya, Y. Hernandez, P.J. King, R.J. Smith, V. Nicolosi, L.S. Karlsson, F.M. Blighe, S. De, W. Zhiming, I.T. McGovern, G.S. Duesberg, J.N. Coleman, Liquid phase production of graphene by exfoliation of graphite in surfactant/water solutions, J. Am. Chem. Soc. 131 (2009) 3611–3620.

[120] Z. Lin, P.S. Karthik, M. Hada, T. Nishikawa, Y. Hayashi, Simple Technique of Exfoliation and Dispersion of Multilayer Graphene from Natural Graphite by Ozone-Assisted Sonication, Nanomaterials. 7 (2017) 125(1)-125(10).

[121] A.S. Pavlova, E.A. Obraztsova, A. V. Belkin, C. Monat, P. Rojo-Romeo, E.D. Obraztsova, Liquid-phase exfoliation of flaky graphite, J. Nanophotonics. 10 (2016) 012525(1)-012525(10).

[122] T. Soltani, B.K. Lee, Low intensity-ultrasonic irradiation for highly efficient, eco-friendly and fast synthesis of graphene oxide, Ultrason. Sonochem. 38 (2017) 693–703.

[123] A.S. Aghdam, F.C. Cebeci, Tailoring the icephobic performance of slippery liquid-infused porous surfaces through the LBL method, Langmuir. 36 (2020) 14145–14154.

[124] R. Lévy, M. Maaloum, Measuring the spring constant of atomic force microscope cantilevers: Thermal fluctuations and other methods, Nanotechnology. 13 (2002) 33–37.

[125] B. V. Derjaguin, V.M. Muller, Y.P. Toporov, Effect of contact deformations on the adhesion of particles, J. Colloid Interface Sci. 53 (1975) 314–326.

[126] E. Ghafari, Y. Feng, Y. Liu, I. Ferguson, N. Lu, Investigating process-structure relations of ZnO nanofiber via electrospinning method, Compos. Part B Eng. 116 (2017) 40–45.

[127] I.M. Joni, L. Nulhakim, M. Vanitha, C. Panatarani, Characteristics of crystalline silica (SiO_2) particles prepared by simple solution method using sodium silicate (Na_2SiO_3) precursor, in: J. Phys. Conf. Ser., Institute of Physics Publishing, (2018) 1-7.

[128] G. Soni, S. Srivastava, P. Soni, P. Kalotra, Y.K. Vijay, Optical, mechanical and structural properties of PMMA/SiO_2 nanocomposite thin films, Mater. Res. Express. 5 (2018) 15302.

[129] H.S. Mansur, R.L. Oréfice, A.A.P. Mansur, Characterization of poly(vinyl alcohol)/poly(ethylene glycol) hydrogels and PVA-derived hybrids by small-angle X-ray scattering and FTIR spectroscopy, Polymer (Guildf). 45 (2004) 7193–7202.

[130] M. Spasova, O. Stoilova, N. Manolova, I. Rashkov, G. Altankov, Preparation of PLLA/PEG Nanofibers by Electrospinning and Potential Applications, J. Bioact. Compat. Polym. 22 (2007) 62–76.

[131] S.R. Valandro, P.C. Lombardo, A.L. Poli, M.A. Horn, M.G. Neumann, C.C.S. Cavalheiro, Thermal properties of poly (methyl methacrylate)/organomodified montmorillonite nanocomposites obtained by in situ photopolymerization, Mater. Res. 17 (2014) 265–270.

[132] M. Wang, A.J. Hsieh, G.C. Rutledge, Electrospinning of poly(MMA-co-MAA) copolymers and their layered silicate nanocomposites for improved thermal properties, Polymer (Guildf). 46 (2005) 3407–3418.
[133] T. Qian, J. Li, W. Feng, H. Nian, Enhanced thermal conductivity of form-stable phase change composite with single-walled carbon nanotubes for thermal energy storage, Sci. Rep. 7 (2017) 1–10.
[134] X.M. Hu, D.M. Wang, W.M. Cheng, G. Zhou, Effect of polyethylene glycol on the mechanical property, microstructure, thermal stability, and flame resistance of phenol-urea-formaldehyde foams, J. Mater. Sci. 49 (2014) 1556–1565.
[135] R. Scaffaro, F. Lopresti, A. Maio, L. Botta, S. Rigogliuso, G. Ghersi, Electrospun PCL/GO-g-PEG structures: Processing-morphology-properties relationships, Compos. Part A Appl. Sci. Manuf. 92 (2017) 97–107.